

# Foundation Models to Unlock Real-World Evidence from Nationwide Medical Claims

Fan Ma<sup>1,\*</sup>, Yuntian Liu<sup>1,\*</sup>, Xiang Lan<sup>1,\*</sup>, Weipeng Zhou<sup>1</sup>, Jun Ni<sup>1</sup>, Mauro Giuffrè<sup>2</sup>, Lingfei Qian<sup>1</sup>,  
Xueqing Peng<sup>1</sup>, Yujia Zhou<sup>1</sup>, Ruey-Ling Weng<sup>1</sup>, Huan He<sup>1</sup>, Lu Li<sup>4</sup>, Huiyuan Wang<sup>5</sup>, Qingyu Chen<sup>1</sup>,  
Andrew Loza<sup>1</sup>, Laila Rasmy<sup>3</sup>, Degui Zhi<sup>3</sup>, Yuan Lu<sup>1,6</sup>, Chenjie Zeng<sup>8</sup>, Joshua C Denny<sup>8,9</sup>, Lee  
Schwamm<sup>1,7</sup>, Daniella Meeker<sup>1</sup>, Lucila Ohno-Machado<sup>1</sup>, Yong Chen<sup>5</sup> and Hua Xu<sup>1,†</sup>

<sup>1</sup>Department of Biomedical Informatics and Data Science, Yale School of Medicine, Yale University,  
New Haven, CT, USA

<sup>2</sup>Department of Medical, Surgical and Health Sciences, Università degli Studi di Trieste, Trieste, Italy

<sup>3</sup>McWilliams School of Biomedical Informatics, UTHealth Houston, Houston, TX, USA

<sup>4</sup>Applied Mathematics and Computational Science Graduate Group, University of Pennsylvania,  
Philadelphia, PA, USA

<sup>5</sup>Department of Biostatistics, Epidemiology and Informatics, Perelman School of Medicine, University of  
Pennsylvania, Philadelphia, PA, USA

<sup>6</sup>Department of Internal Medicine (Section of Cardiovascular Medicine), Yale School of Medicine, Yale  
University, New Haven, CT, USA

<sup>7</sup>Department of Neurology, Yale School of Medicine, Yale University, New Haven, CT, USA

<sup>8</sup>Precision Health Informatics Section, National Human Genome Research Institute, National Institutes  
of Health, Bethesda, MD, USA

<sup>9</sup>All of Us Research Program, National Institutes of Health, Bethesda, MD, USA

\*Co-first authors      †Corresponding author

Hua Xu: hua.xu@yale.edu

Evidence derived from large-scale real-world data (RWD) is increasingly informing regulatory evaluation and clinical decision-making. Among major RWD sources, administrative claims data provide population-scale, longitudinal records of healthcare utilization, expenditure, and detailed coding of diagnoses, procedures, and medications, yet their potential as a substrate for healthcare foundation models remains largely unexplored. Here we present **ReClaim**, a generative transformer trained from scratch on 43.8 billion medical events from more than 200 million enrollees in the MarketScan claims data spanning 2008–2022. ReClaim models longitudinal healthcare trajectories across diagnoses, procedures, medications, and expenditure, and was scaled to 140 million, 700 million and 1.7 billion parameters. Leveraging large-scale pretraining and task-specific post-training, ReClaim learns representations that generalize across multiple datasets and adapt to diverse downstream healthcare analytic tasks. Across over 1,000 disease-onset prediction tasks, ReClaim achieved a mean AUC of 75.6%, substantially outperforming strong baselines, including disease-specific models based on LightGBM (66.3%) and the transformer-based Delphi model (69.4%), with the largest gains observed for rare diseases. These advantages were consistent across retrospective and prospective evaluations and persisted in external validation across two independent datasets. Performance improved monotonically with model scale, and post-training yielded an absolute gain of 13.8 percentage points over pre-training alone. Beyond disease prediction, ReClaim demonstrates broader real-world applicability by capturing financial outcomes and improving robustness in real-world evidence (RWE) generation. For healthcare expenditure forecasting, it increased explained variance ( $R^2$ ) from 0.28 to 0.37 relative to a LightGBM baseline. In a target trial emulation study, it reduced systematic bias by 72% on average relative to Delphi. Together, these results establish nationwide medical claims as a scalable substrate for healthcare foundation models and demonstrate that learned representations generalize across time periods and data sources, supporting diverse downstream tasks including disease prediction, expenditure forecasting, and RWE generation.

# 1 Introduction

Real-world data (RWD) capturing healthcare delivered in routine practice have become indispensable for complementing randomized controlled trials (RCTs) in regulatory evaluation, clinical decision-making, and health policy development [1, 2, 3, 4]. Among sources of RWD, electronic health records (EHRs) and administrative claims data both capture essential records of healthcare encounters, including diagnoses, procedures, and prescriptions, but differ in their structure and scope. EHRs provide detailed clinical information, such as laboratory results, imaging, and clinical notes, but records are often incomplete because patients may receive care across multiple health systems and EHRs lack a defined observation window, making unrecorded events difficult to distinguish from true absence and introducing false-negative bias [5]. In contrast, administrative claims data lack granular clinical detail [2], but provide complete and standardized longitudinal records of patients’ disease trajectories and treatment histories, along with comprehensive capture of healthcare utilization and expenditures across large populations, ensuring continuity across providers within payer systems [5]. Defined enrollment periods further anchor observation windows, enabling more reliable interpretation of healthcare utilization over time. These two complementary and ever-growing data sources position RWD as a powerful basis for modeling longitudinal healthcare trajectories in real-world settings.

Building on this potential, there has been growing interest in developing foundation models trained on large-scale RWD. Early work, including BEHRT [6] and Med-BERT [7], demonstrated that structured EHRs can be represented as sequences of clinical events forming longitudinal healthcare trajectories, enabling transformer-based models to learn transferable representations and improve disease prediction tasks [8, 9]. More recent studies [10, 11, 12, 13] extend this paradigm to generative modeling of health event trajectories, enabling time-to-event forecasting, simulation of longitudinal healthcare pathways, and zero- or few-shot adaptation across outcomes, as exemplified by models such as Foresight [14] and ETHOS [15]. In parallel, increasing emphasis has been placed on systematic benchmarking and scaling: Delphi [16] demonstrates strong performance in modeling the incidence of more than 1,000 diseases, approaching the accuracy of specialized single-disease models despite relatively modest data and model scale, while the large-scale Curiosity study [17] shows that predictive performance improves consistently with increasing dataset and model size across diverse tasks, highlighting scaling as a key pathway toward more generalizable healthcare foundation models [18].

Despite recent progress, the real-world applicability of foundation models trained on RWD remains constrained by limited generalizability across populations, data sources, and tasks. First, data scale and coverage remain limited: most models are trained on single health systems or modest-sized cohorts, limiting their ability to capture heterogeneous healthcare trajectories at scale and generalize across diverse settings and temporal contexts [16, 19]. Second, the field remains largely EHR-centric: most models are developed and evaluated within EHR data, while claims-based modeling remains underexplored and cross-source validation is rare, constraining robustness and generalizability across varied real-world settings [20, 21]. Third, despite the multipotency of these models, the scope of evaluation tasks has been narrow, with most studies focusing on disease-specific prediction benchmarks, limiting the ability of learned representations to generalize across the broader spectrum of tasks required to capture healthcare dynamics and enable evidence generation [3, 22]. Fourth, the limited exploration of post-training strategies for task-specific adaptation constrains the ability of models to generalize effectively to more complex downstream problems. Collectively, these limitations hinder the development of foundation models capable of capturing the full spectrum of longitudinal healthcare processes, limiting its readiness for robust deployment in real-world research and practice.

Here we present ReClaim, a healthcare foundation model that advances generalization across nationwide populations, data sources, and tasks. Developed on 43.8 billion claims records from more than 200 million enrollees in the U.S. MarketScan databases spanning 2008–2022, ReClaim models comprehensive longitudinal healthcare trajectories, jointly capturing clinical and financial outcomes. It establishes an end-to-end framework that integrates large-scale pretraining with task-specific post-training to learn transferable representations and enable adaptation to complex prediction tasks across more than 1,000 diseases. We show that ReClaim consistently outperforms strong baselines across heterogeneous evaluation regimes, including both in-domain (Claims) and out-of-domain (EHRs), retrospective (2008–2022) and prospective (2023 onward) settings, as different aspects of generalizability assessments. Beyond disease-focused benchmarks, ReClaim extends to clinically and economically meaningful tasks, including healthcare expenditure forecasting and identification

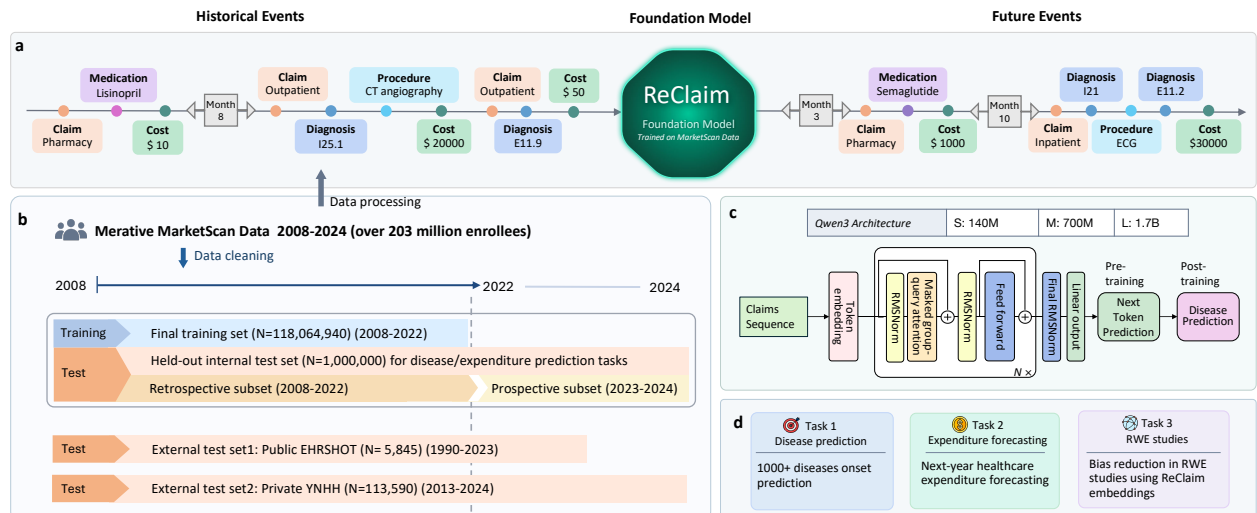


**Figure 1 | ReClaim framework and evaluation workflow.** (a), Longitudinal medical events from patient claims are encoded as chronologically ordered trajectories, and the ReClaim foundation model autoregressively predicts future medical events including diagnoses, procedures, medications, and expenditure. (b), The study datasets comprise the MarketScan corpus partitioned into a final training set, a held-out internal test cohort for disease and expenditure prediction with retrospective and prospective temporal subsets, and two external testing datasets: EHRShot and Yale New Haven Health (YNHH). This partitioning and external sources enable four testing scenarios. (c), Transformer-based ReClaim models (Qwen3 architecture) are trained at three parameter scales (S: 140M, M: 700M, L: 1.7B) through next-token pre-training, followed for disease onset prediction by task-specific post-training. (d), ReClaim is evaluated on three downstream tasks: disease onset prediction for over 1,000 International Classification of Diseases, Tenth Revision, Clinical Modification (ICD-10-CM) conditions, next-year healthcare expenditure forecasting, and RWE applications including propensity score modeling using ReClaim embeddings.

of high-need, high-cost subgroups, linking clinical risk with financial burden. Moreover, it improves the robustness of observational RWE studies: representations learned by ReClaim enhance propensity score estimation, leading to substantial reductions in residual bias in target trial emulation analyses, demonstrating its utility for reliable RWE generation.

## 2 Results

### 2.1 ReClaim Overview and Evaluation Benchmarks

ReClaim converts longitudinal claims records into chronologically ordered patient trajectories that jointly encode enrollment history, clinical events, and healthcare expenditures (Fig. 1a). These trajectories were used to train decoder-only Transformer models from scratch at three parameter scales with a next-token prediction objective, followed by task-specific post-training for disease onset prediction. For clarity, we denote the three pre-trained model variants as ReClaim-S (140M), ReClaim-M (700M), and ReClaim-L (1.7B), and the post-trained large model as ReClaim.

ReClaim was first pre-trained on over 118 million filtered claims records collected between 2008 and 2022, and was subsequently evaluated on three downstream task categories across four benchmarks (Fig. 1b; Supplementary Table A2). The evaluation benchmarks included a one-million held-out MarketScan cohort, consisting of a retrospective subset (2008–2022) and a prospective subset (2023 onward) to assess temporal generalization, as well as two external EHR-based cohorts: EHRShot [13] and Yale New Haven Health (YNHH). The three task categories comprised: (1) *disease onset prediction* for over 1,000 ICD-10-CM conditions, evaluated across all benchmarks; (2) *healthcare expenditure forecasting*, measured as next-year total gross payments and including identification of high-need, high-cost individuals, evaluated on the predictive cohort; and (3) *RWE analyses*, assessing whether ReClaim-derived representations improve confounding

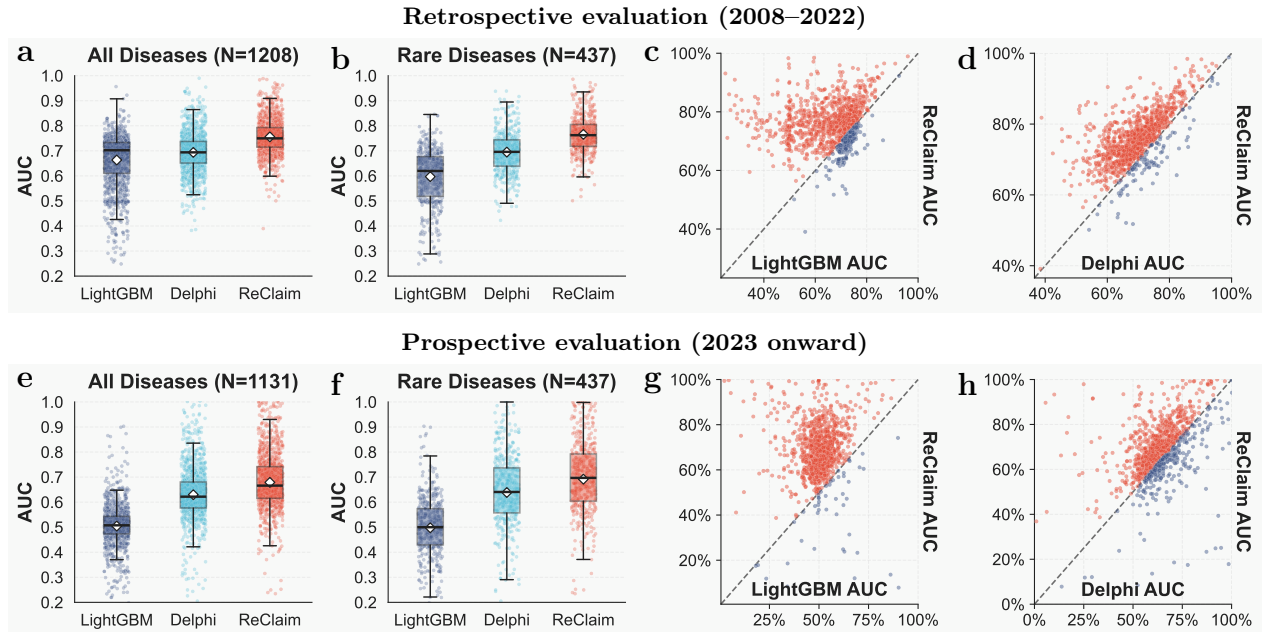


**Figure 2 | ReClaim outperforms LightGBM and Delphi across disease endpoints.** Top row, retrospective held-out evaluation on the 2008–2022 split; bottom row, prospective temporal evaluation on the post-2023 cohort. Statistical comparisons use paired disease-level AUC differences, reported as mean  $\Delta$  with 95% bootstrap confidence intervals (CI) and Holm-adjusted two-sided paired Wilcoxon signed-rank  $P$  values. (a), Distribution of disease-level AUC for ReClaim, Delphi, and LightGBM across 1,208 shared disease endpoints, shown as box plots with overlaid jittered scatter; diamonds indicate group means. Mean AUC: ReClaim = 75.57%, Delphi = 69.36%, LightGBM = 66.34%. (b), Same comparison restricted to a rare-disease subset of 437 endpoints (prevalence < 0.0005,  $n_{\text{diseased}} > 10$ ); ReClaim exceeded LightGBM by +16.87 pp (95% CI, 15.76–18.04;  $P_{\text{Holm}} = 1.9 \times 10^{-70}$ ) and Delphi by +7.07 pp (95% CI, 6.49–7.68;  $P_{\text{Holm}} = 1.4 \times 10^{-61}$ ). (c), Per-disease paired scatter of ReClaim AUC versus LightGBM AUC; points above the diagonal indicate diseases where ReClaim outperforms LightGBM (79.9% of endpoints; mean  $\Delta = +9.23$  pp; 95% CI, 8.56–9.91;  $P_{\text{Holm}} = 9.5 \times 10^{-126}$ ). (d), Per-disease paired scatter of ReClaim AUC (orange) versus Delphi AUC (blue); ReClaim (orange) exceeds Delphi (blue) in 92.0% of diseases (mean  $\Delta = +6.21$  pp; 95% CI, 5.88–6.56;  $P_{\text{Holm}} = 1.1 \times 10^{-161}$ ). e–h, Same four panel types under prospective temporal evaluation (shared test cohort; 1,131 disease endpoints with paired AUC for all three models). (e), Distribution of prospective disease-level AUC. Mean AUC: ReClaim = 67.89%, Delphi = 62.97%, LightGBM = 50.44%. (f), Same rare-disease subset of 437 endpoints; ReClaim exceeded LightGBM by +19.42 pp (95% CI, 17.55–21.32;  $P_{\text{Holm}} = 1.0 \times 10^{-56}$ ) and Delphi by +5.34 pp (95% CI, 3.67–7.02;  $P_{\text{Holm}} = 2.0 \times 10^{-14}$ ). (g), ReClaim versus LightGBM paired scatter (95.8% of endpoints above the diagonal; mean  $\Delta = +17.46$  pp; 95% CI, 16.61–18.30;  $P_{\text{Holm}} = 2.6 \times 10^{-167}$ ). (h), ReClaim versus Delphi paired scatter (77.0% above the diagonal; mean  $\Delta = +4.93$  pp; 95% CI, 4.20–5.65;  $P_{\text{Holm}} = 2.2 \times 10^{-70}$ ).

adjustment in a target trial emulation case study.

## 2.2 Disease Onset Prediction

Disease onset prediction was assessed by using each patient’s historical trajectory up to the prediction time to generate disease-specific scores for incident events in a future window beginning at least one year after the prediction time, spanning 1,208 ICD-10-CM disease endpoints. ReClaim followed the evaluation protocol of Delphi [16] and was benchmarked against both Delphi [16] and 1,208 disease-specific LightGBM models [23]. Rare diseases were defined using a prevalence threshold of no more than 5 per 10,000 individuals [24]. As not all datasets contained all endpoints, the number of evaluable diseases varied across the retrospective held-out, prospective temporal, and external EHR-based evaluations. Performance in each test set was summarized by disease-level ROC-AUC, and cross-model comparisons were restricted to harmonized endpoints available for all methods being compared.

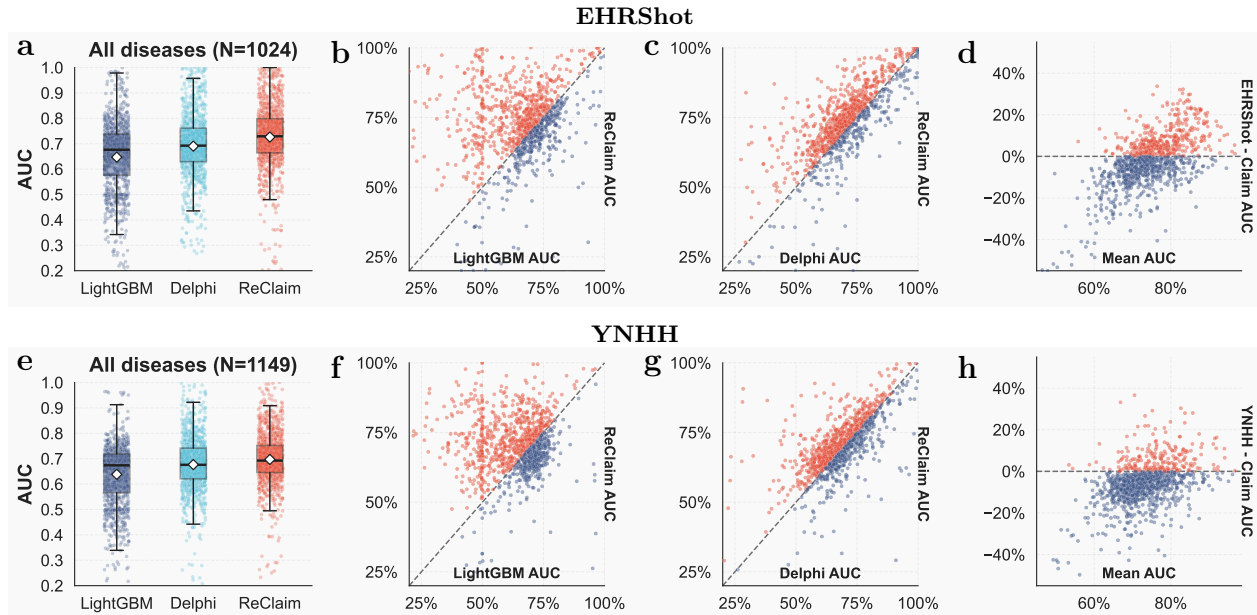


**Figure 3 | External validation on EHR-based datasets.** Top row, EHRShot; bottom row, YNHH. Statistical comparisons use paired disease-level AUC differences, reported as mean  $\Delta$  with 95% bootstrap confidence intervals (CI) and Holm-adjusted two-sided paired Wilcoxon signed-rank  $P$  values. (a), Disease-level AUC distributions across all diseases shared by LightGBM, Delphi, and ReClaim in the EHRShot cohort (1,024 shared disease endpoints). Mean AUC: ReClaim = 72.64%, Delphi = 69.03%, LightGBM = 64.72%. (b), Per-disease paired scatter of ReClaim AUC (orange) versus LightGBM AUC on EHRShot; points above the diagonal indicate diseases where ReClaim outperforms LightGBM (64.7% of endpoints; mean  $\Delta = +7.92$  pp; 95% CI, 6.78–9.08;  $P_{\text{Holm}} = 5.9 \times 10^{-37}$ ). (c), Per-disease paired scatter of ReClaim AUC versus Delphi AUC on EHRShot; ReClaim exceeds Delphi in 72.9% of diseases (mean  $\Delta = +3.61$  pp; 95% CI, 3.03–4.19;  $P_{\text{Holm}} = 7.9 \times 10^{-48}$ ). (d), Per-disease difference in ReClaim AUC between EHRShot and MarketScan retrospective set across the same 1,024 diseases, plotted against the mean AUC across datasets (mean  $\Delta = -2.78$  pp; 95% CI, -3.62 to -1.96;  $P_{\text{Holm}} = 3.4 \times 10^{-10}$ ). e–h, Same four panel types in the YNHH cohort. (e), Disease-level AUC distributions across 1,149 diseases shared by LightGBM, Delphi, and ReClaim. Mean AUC: ReClaim = 69.70%, Delphi = 67.69%, LightGBM = 63.83%. (f), ReClaim versus LightGBM paired scatter (59.3% of endpoints above the diagonal; mean  $\Delta = +5.88$  pp; 95% CI, 4.99–6.76;  $P_{\text{Holm}} = 4.0 \times 10^{-27}$ ). (g), ReClaim versus Delphi paired scatter (62.9% above the diagonal; mean  $\Delta = +2.02$  pp; 95% CI, 1.46–2.58;  $P_{\text{Holm}} = 1.7 \times 10^{-22}$ ). (h), Per-disease difference in ReClaim AUC between YNHH and MarketScan retrospective set across the same 1,149 diseases, plotted against the mean AUC across datasets (mean  $\Delta = -5.87$  pp; 95% CI, -6.48 to -5.29;  $P_{\text{Holm}} = 5.1 \times 10^{-88}$ ).

**Retrospective evaluation (2008–2022)** In the 1-million retrospective held-out cohort, ReClaim showed a broad improvement over both baselines, with the highest disease-level AUC distribution across 1,208 shared endpoints (Fig. 2a). The gain was especially evident for rare diseases, where LightGBM degraded more sharply and ReClaim retained discrimination across low-prevalence endpoints (Fig. 2b). Paired disease-level analyses showed that these improvements were not confined to a small subset of conditions: ReClaim outperformed LightGBM and Delphi across most endpoints, with gains distributed over the full performance range (Fig. 2c,d).

**Prospective evaluation (2023 onward)** The advantage persisted under temporal shift. In the post-2023 cohort, ReClaim again achieved the strongest overall discrimination across the shared disease endpoints (Fig. 2e–h). The separation from LightGBM was larger in this prospective setting, while the comparison with Delphi remained consistently favorable. Together, the retrospective and prospective analyses indicate that claims-scale sequence pre-training yields disease-risk estimates that are both more accurate and more temporally robust than supervised endpoint-specific models and the disease-sequence language-model comparator.

**External validation** We next tested whether a claims-trained model could transfer to EHR-derived cohorts after harmonizing records into the same trajectory format. On both EHRShot [13] and YNHH, ReClaim-L retained the highest disease-level AUC distributions among the three models (Fig. 3a,e). Paired comparisons

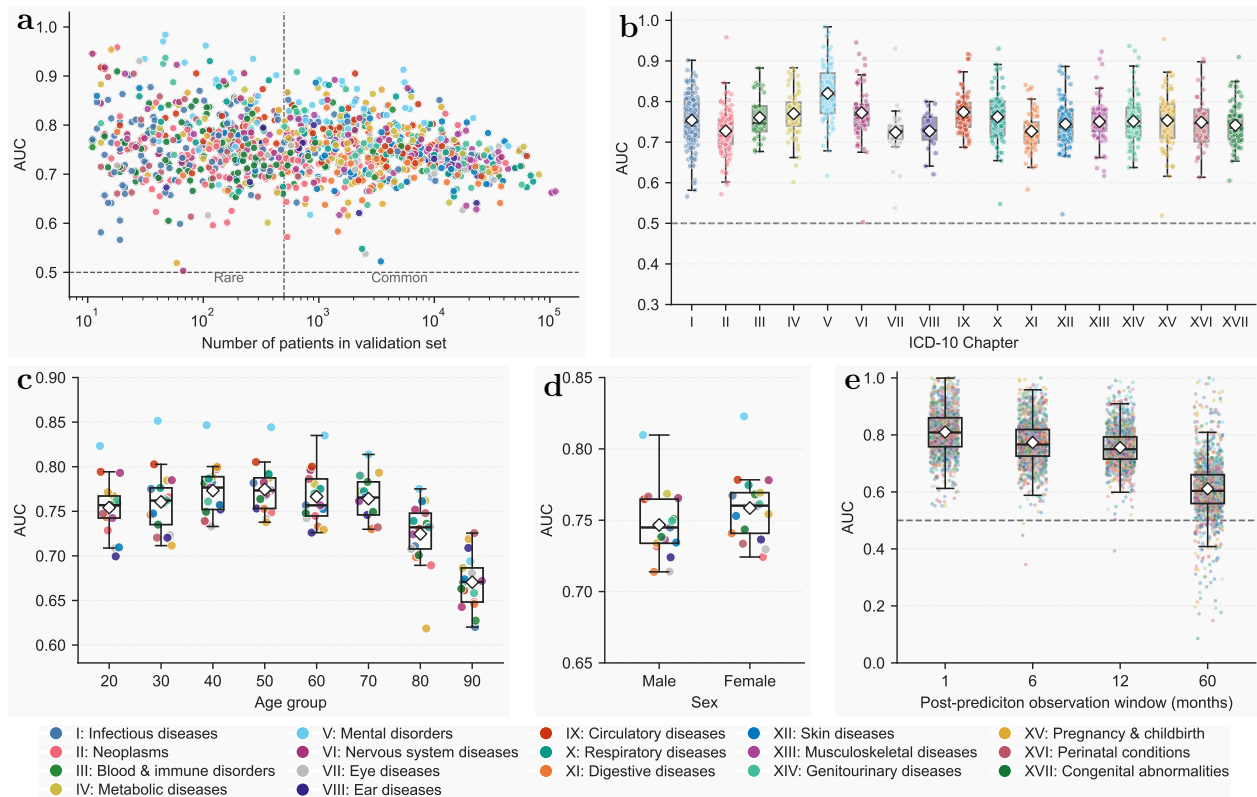


**Figure 4 | Discrimination performance across disease prevalence, clinical domain, demographic, and temporal strata.** (a), Disease-level AUC as a function of the number of diseased patients in the retrospective held-out set, with each point representing one of 1,141 disease endpoints coloured by ICD-10; dashed lines mark the chance level (AUC = 0.5) and the rare-disease boundary. Overall mean disease-level AUC = 75.38% (median = 74.93%); 83.7% of endpoints exceed AUC 0.70 and 20.0% exceed AUC 0.80. Rare endpoints ( $n = 457$ ) reach a higher mean AUC of 76.48% than common endpoints ( $n = 684$ ; 74.64%). (b), Per-chapter AUC distributions across all 17 ICD-10 chapters, shown as box plots with overlaid individual disease AUC values. The strongest chapter is V. Mental Disorders (mean AUC = 82.03%), followed by IX. Circulatory (77.40%), VI. Nervous System (77.23%), and IV. Metabolic (76.99%); the weakest are VII. Eye (72.41%), XI. Digestive (72.68%), and VIII. Ear (72.74%). (c), Category-level mean AUC stratified by patient age group (20–90 years, in decades). Mean AUC peaks in the 50s decade (77.62%) and declines in the oldest groups (80s = 72.67%; 90s = 66.25%). (d), Category-level mean AUC stratified by sex (female = 75.96%; male = 74.72%). (e), Disease-level AUC across prediction-to-diagnosis post-prediction observation windows of 1, 6, 12 and 60 months, with individual disease points coloured by ICD-10 chapter. Mean AUC declines monotonically with horizon: 1 month = 80.99%, 6 months = 77.30%, 12 months = 75.57%, 60 months = 61.08%. Diamonds indicate group means in all box plots.

remained favorable against LightGBM and Delphi in both cohorts (Fig. 3b,c,f,g), although absolute performance was attenuated relative to in-domain claims testing (Fig. 3d,h). These findings suggest that the learned claims representations capture portable longitudinal disease structure while still reflecting expected dataset shift between administrative claims and EHR data. Two compounding shifts account for this gap: hospital-based recruitment in EHRShot and YNHH yields per-disease prevalence  $2.95 \times$  and  $1.49 \times$  that of MarketScan across 1,013 overlapping endpoints (Supplementary Table A5), and EHR records differ from claims in coding granularity, capture mechanism and event timing, together altering the trajectory distribution at inference.

**Discrimination across disease, demographic, and temporal strata** We further examined whether discrimination varied with endpoint prevalence, clinical domain, patient demographics and prediction horizon (Fig. 4a–e). Across 1,141 evaluable diseases, ReClaim-L achieved consistently useful discrimination, with most endpoints exceeding an AUC of 0.70 (Fig. 4a). Rare diseases showed greater variability, whereas common

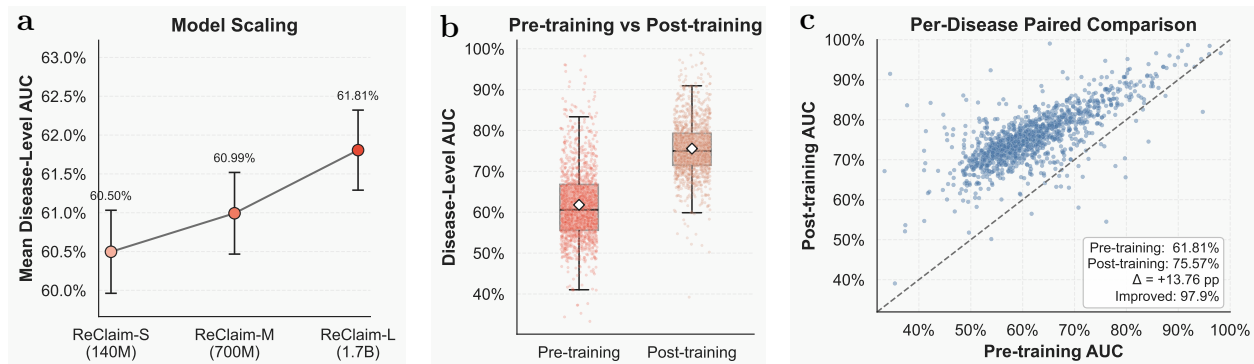


**Figure 5 | Scaling and post-training improve disease onset prediction.** (a), Disease onset prediction improves monotonically with model scale; mean AUC rises from 60.50% (ReClaim-S) to 60.99% (ReClaim-M) and 61.81% (ReClaim-L) across 1,208 shared disease endpoints. (b), Distribution of disease-level AUC before (pre-training) and after (post-training), shown as box plots with overlaid jittered scatter; diamonds indicate group means. Mean AUC increases from 61.81% (pre-training, ReClaim-L) to 75.57% (post-training, ReClaim-L). (c), Per-disease paired scatter of pre-training versus post-training AUC across 1,208 shared endpoints; points above the diagonal indicate diseases where post-training improves performance (97.9% of endpoints; mean  $\Delta = +13.76$  pp; 95% CI, 13.41–14.11;  $P = 7.1 \times 10^{-195}$ , two-sided paired Wilcoxon signed-rank test).

endpoints converged to a narrower high-performance band.

Performance varied across ICD-10 chapters, with stronger discrimination for chronic disease domains whose trajectories are reflected in repeated utilization patterns and lower discrimination for domains more dependent on acute presentation, imaging or histological confirmation (Fig. 4b). This heterogeneity is consistent with the information content available in longitudinal claims rather than a uniform model failure across disease groups.

Discrimination was broadly stable across age and sex strata (Fig. 4c,d). The main demographic attenuation appeared in the oldest age groups, where multimorbidity and competing risks likely make incident disease labels less separable from background utilization.

As expected, performance decreased as the prediction horizon lengthened, but discrimination remained above chance for most diseases even at five years (Fig. 4e). The trajectory representation therefore supports both near-term risk stratification and longer-term disease forecasting, with temporal decay behaving as an empirical property of the task rather than a failure of calibration alone.

**Model scaling and post-training** Disease-level discrimination improved monotonically with model size before task-specific post-training (Fig. 5a). Although the absolute scaling gains were modest, they were distributed across many endpoints, indicating a systematic benefit from increasing model capacity rather than an improvement driven by a few high-prevalence diseases.

Task-specific post-training produced a much larger shift, moving nearly the entire disease-level AUC distribution upward (Fig. 5b,c). This pattern suggests that claims-scale pre-training learns a general longitudinal health representation, while supervised post-training aligns that representation with incident-disease risk across the disease spectrum.

## 2.3 Healthcare Expenditure Forecasting

We next evaluated whether large-scale pre-training improved forecasting of next-year healthcare expenditure, measured as total gross payment to all providers in the subsequent calendar year. Performance was assessed in the held-out predictive cohort under three complementary settings: continuous regression of total expenditure; three-class expenditure stratification using \$1,500 and \$15,000 cutoffs; and high-need, high-cost identification using a \$30,000 cutoff. In our pooled population, these cutoffs mapped to the 44th, 91st and 95.6th percentiles, closely matching the reference percentile thresholds in Supplementary Table A10.

**Retrospective evaluation (2008–2022)** In the retrospective subset, ReClaim outperformed the LightGBM

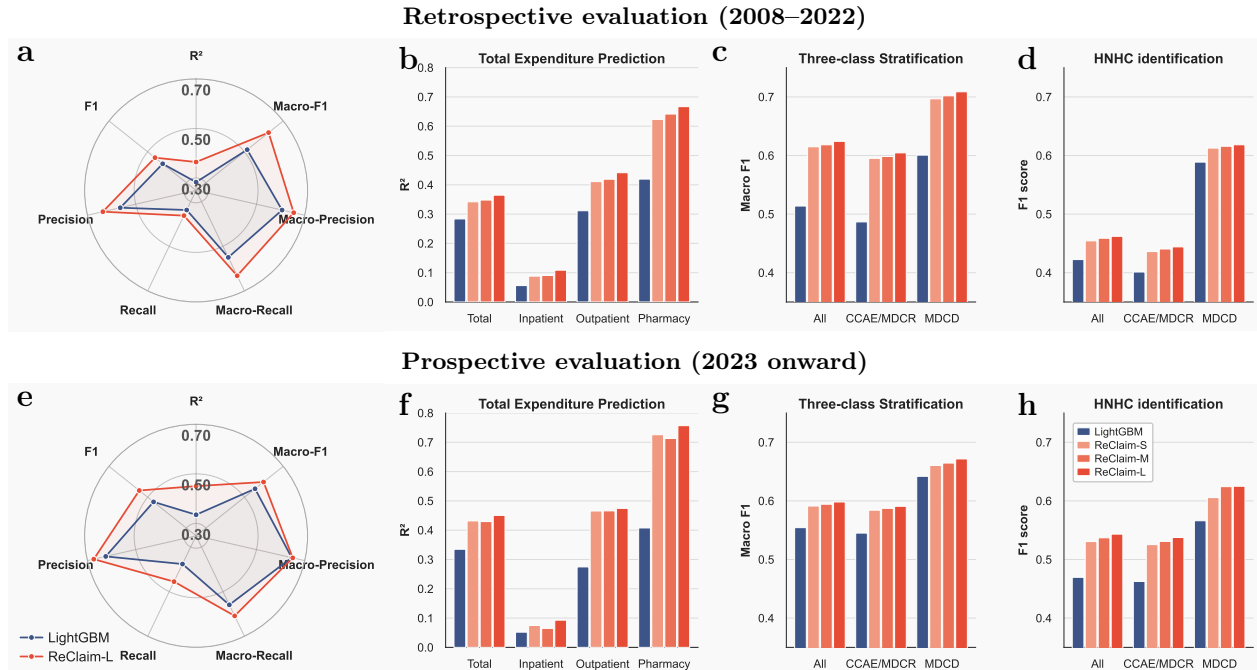


**Figure 6 | ReClaim improves next-year healthcare expenditure forecasting.** Top row, retrospective held-out evaluation on the 2008–2022 split; bottom row, prospective temporal evaluation on the post-2023 cohort. Expenditure was measured as next-year total gross payment to all providers. Three task settings were evaluated: regression of total expenditure; three-class expenditure stratification using thresholds of \$1,500 and \$15,000; and binary high-need, high-cost (HNHC) identification using a threshold of \$30,000. (a), Radar plot summarizing retrospective performance across regression, stratification and HNHC metrics. (b), Retrospective total expenditure regression. ReClaim-L reduced MAE from 5,871 for LightGBM to 4,982, a 15.1% reduction, and increased  $R^2$  from 0.2835 to 0.365, a 28.6% relative improvement. Across ReClaim scales, MAE decreased from 5,115 for ReClaim-S to 4,982 for ReClaim-L, while  $R^2$  increased from 0.342 to 0.365. (c), Retrospective three-class stratification. ReClaim-L improved accuracy from 0.529 to 0.660 and macro F1 from 0.514 to 0.624 relative to LightGBM, with gains in macro precision from 0.606 to 0.654 and macro recall from 0.550 to 0.632. (d), Retrospective HNHC identification. ReClaim-L increased F1 from 0.422 to 0.462, precision from 0.564 to 0.636 and recall from 0.338 to 0.363 relative to LightGBM. (e), Radar plot summarizing prospective performance under the same task definitions and thresholds. (f), Prospective total expenditure regression. ReClaim-L reduced MAE from 7,881 to 7,293, a 7.5% reduction, and increased  $R^2$  from 0.335 to 0.451, a 34.6% relative improvement. Across ReClaim scales, MAE decreased from 7,440 for ReClaim-S to 7,293 for ReClaim-L, while  $R^2$  increased from 0.432 to 0.451. (g), Prospective three-class stratification. ReClaim-L improved accuracy from 0.571 to 0.600 and macro F1 from 0.554 to 0.598 relative to LightGBM, with macro recall increasing from 0.542 to 0.598. (h), Prospective HNHC identification. ReClaim-L increased F1 from 0.470 to 0.543, precision from 0.627 to 0.670 and recall from 0.376 to 0.455 relative to LightGBM.

baseline across all three expenditure tasks (Fig. 6a–d). For total expenditure regression, ReClaim-L achieved lower prediction error and higher explained variance than LightGBM (Fig. 6a,b). The same pattern extended to clinically useful risk stratification: ReClaim-L improved three-class expenditure prediction and high-need, high-cost identification, with gains distributed across precision and recall rather than driven by a single metric (Fig. 6c,d). Performance also improved consistently from ReClaim-S to ReClaim-L, indicating modest but systematic scaling benefits beyond the overall separation from LightGBM.

**Prospective evaluation (2023 onward)** The advantage persisted under temporal generalization. In the post-2023 prospective subset, ReClaim-L again outperformed LightGBM across regression, three-class stratification and high-need, high-cost identification (Fig. 6e–h). Improvements were particularly evident for explained variance in total expenditure and for recall in identifying high-need, high-cost individuals, suggesting that sequence pre-training captured longitudinal utilization patterns associated with future high-cost care.

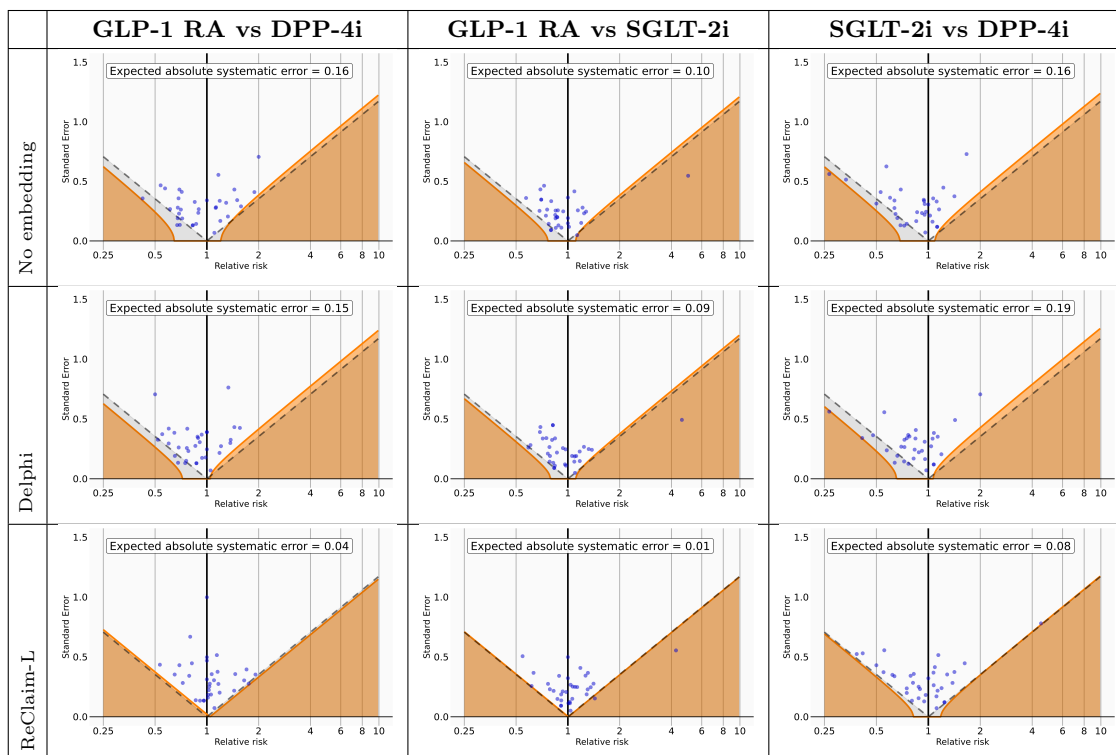


**Figure 7 | Relative risk and expected absolute systematic error (EASE) of negative control outcomes (NCOs) after propensity matching across pairwise treatment comparisons.** Analyses were performed in 7,246 eligible individuals from the one-million-person held-out RWE cohort. Columns represent pairwise treatment comparisons among GLP-1 RAs, SGLT-2is and DPP-4is, while rows denote the covariate specification used for propensity score estimation: conventional clinical covariates without learned embeddings, covariates augmented with Delphi embeddings and covariates augmented with ReClaim-L embeddings. Each panel shows relative risk estimates for NCOs after propensity score matching; points closer to the null indicate lower residual systematic bias. EASE summarizes the average absolute systematic error across NCOs, with lower values indicating better bias control. For GLP-1 RA versus DPP-4i, EASE decreased from 0.16 without embeddings to 0.15 with Delphi and 0.04 with ReClaim-L. For GLP-1 RA versus SGLT-2i, EASE was 0.10 without embeddings, 0.09 with Delphi and 0.01 with ReClaim-L. For SGLT-2i versus DPP-4i, EASE was 0.16 without embeddings, 0.19 with Delphi and 0.08 with ReClaim-L.

Similar to the retrospective setting, performance generally increased with model scale, with ReClaim-L achieving the best overall results across prospective tasks.

**Stratification across payer and claim-type strata** Stratified analyses showed that the superiority of large-scale pre-training over supervised modelling for expenditure forecasting was not limited to the overall population, but extended across payer groups and claim types. ReClaim achieved broadly consistent gains across strata, with stronger performance for pharmacy expenditure and weaker performance for inpatient expenditure, reflecting differences in the regularity and predictability of utilization patterns across claim types. Across payer groups, ReClaim improved performance in all strata, with larger gains in Medicaid than in commercial and Medicare supplemental populations (Fig. 6). Scaling trends were generally preserved across strata, but remained smaller than the overall gains over LightGBM.

## 2.4 Support for Real-World Evidence Analyses

We evaluated whether ReClaim-derived representations improve confounding adjustment in an observational RWE setting using an embedding-augmented target trial emulation comparing three antidiabetic drug classes for psychiatric outcomes. Pairwise comparisons among glucagon-like peptide-1 receptor agonists (GLP-1 RAs), sodium-glucose cotransporter-2 inhibitors (SGLT-2is) and dipeptidyl peptidase-4 inhibitors (DPP-4is)

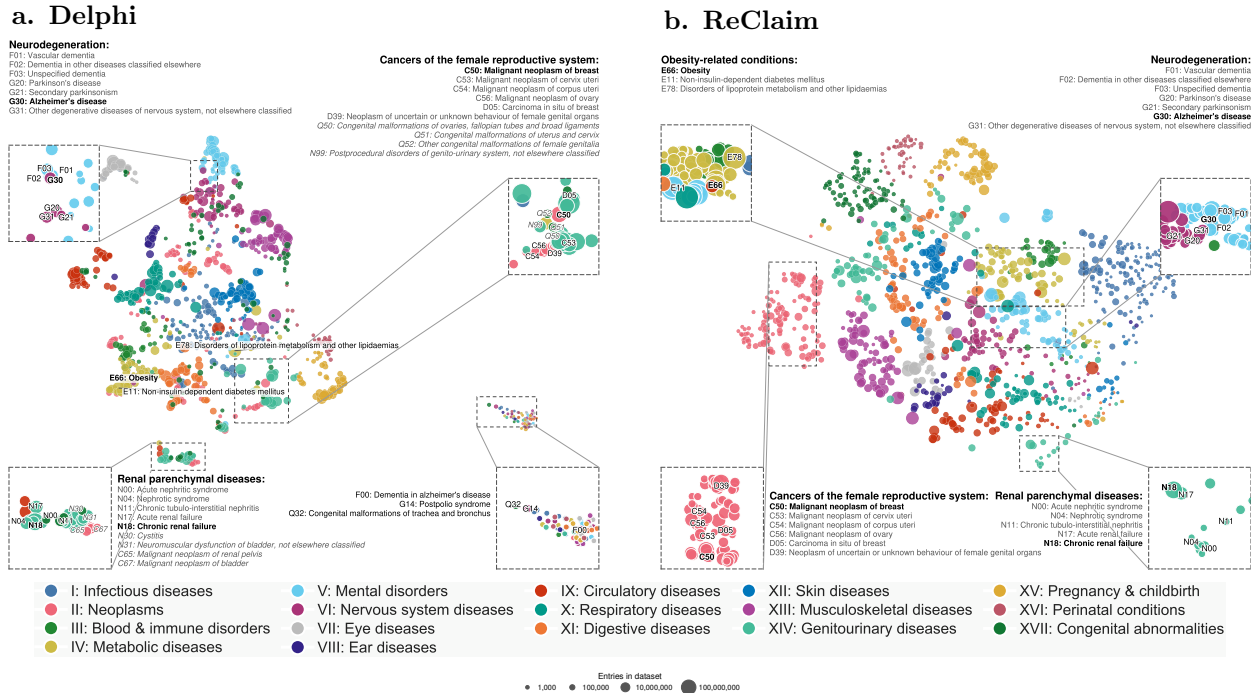


**Figure 8 | Uniform Manifold Approximation and Projection (UMAP) of learned disease embeddings. a, Delphi. b, ReClaim.** Each point denotes an ICD-10 disease token projected from the pretrained embedding space to two dimensions. Colors indicate ICD-10 chapter groups and marker size reflects token frequency in the training corpus. Relative to Delphi, ReClaim showed tighter local neighborhoods and clearer chapter-level structure while preserving continuity between clinically related disease systems.

were conducted using 1:1 propensity score matching based on either conventional clinical covariates alone or covariates augmented with learned embeddings. Residual systematic bias was quantified using expected absolute systematic error (EASE) estimated from negative control outcomes (NCOs) that share bias structure with the outcomes of interest but are not causally related to treatment.

A total of 7,246 eligible individuals were identified from the 1 million held-out RWE cohort. Propensity score distributions showed adequate overlap, with most individuals within the empirical equipoise range (Supplementary Fig. A2), indicating acceptable comparability between treatment groups after matching. Despite this overlap, residual systematic error differed across modeling strategies. Baseline and Delphi-augmented models yielded more dispersed negative-control relative risk estimates, whereas ReClaim-augmented models produced estimates more tightly centered around the null (Fig. 7).

These differences were reflected in EASE across all three pairwise treatment comparisons (Fig. 7). ReClaim-L consistently produced the lowest residual systematic bias relative to conventional covariates alone and Delphi-derived embeddings, indicating improved adjustment for latent confounding structure. Calibrated treatment effect estimates for primary psychiatric outcomes across specifications are reported in Supplementary Table A16. Overall, these results indicate that ReClaim-derived embeddings improve adjustment for latent confounders beyond structured variables, consistently reduce residual systematic error across treatment comparisons, and enable more robust causal estimation in observational RWE analyses.

## 2.5 Visualization of Learned Representation

The pretrained disease embedding spaces of Delphi and ReClaim were visualized with UMAP (Fig. 8). Delphi produced a relatively diffuse arrangement, whereas ReClaim showed clearer large-scale organization. In the ReClaim map, major ICD-10 chapters occupied distinct regions, and clinically related conditions formed compact local neighborhoods, indicating that pre-training on large-scale claims trajectories organizes diseases

by both semantic similarity and shared longitudinal context. Common disease endpoints were concentrated near the centers of chapter-level clusters, whereas rarer diagnoses were more often located at the periphery or in smaller satellite groups, consistent with a hierarchy extending from broad disease families to finer subtypes. The ReClaim manifold was not separated strictly by chapter. Selected groups showed partial continuity, including metabolic and cardiovascular disorders as well as respiratory and infectious diseases, suggesting that the model captures recurring cross-chapter relationships within ICD-10 that arise in routine care trajectories. Compared with Delphi’s narrower disease-focused representation, ReClaim appeared to encode a broader view of longitudinal health states by integrating diagnoses, procedures, medications, and expenditure signals.

### 3 Discussion

In this study, we present ReClaim, a healthcare foundation model trained on nationwide medical claims data, and demonstrate its ability to learn transferable representations that generalize across diseases, tasks, time periods, and data sources. Across more than 1,000 disease onset prediction tasks, healthcare expenditure forecasting, and RWE analyses, ReClaim consistently outperforms gradient-boosted tree and transformer-based baselines. These results establish administrative claims as a scalable and effective substrate for healthcare foundation models and highlight the potential of large-scale RWD to support diverse downstream applications.

A central contribution of this work is the demonstration that administrative claims data, despite lacking the granular clinical detail of EHRs, can support robust representation learning across multiple dimensions of generalization. Whereas EHRs are often fragmented across care settings and health systems, claims data provide standardized records of healthcare utilization with longitudinal continuity across providers during payer-defined enrollment periods. This structure provides a coherent view of observable care trajectories, reducing ambiguity between the absence of recorded events and incomplete capture. The strong performance achieved across disease prediction evaluations, including rare conditions, retrospective and prospective evaluation, and external validation, suggests that ReClaim learns patterns of disease burden and healthcare utilization that are not limited to highly prevalent conditions, a restricted time period, or a single data source, supporting the broader generalizability of claims-derived representations across heterogeneous real-world settings.

Beyond predictive performance, ReClaim extends the scope of healthcare foundation models to encompass economically and clinically meaningful tasks. The ability to jointly model diagnoses, procedures, medications, and expenditure enables a unified representation of patient trajectories that links clinical risk with healthcare utilization and financial burden. Improvements in expenditure forecasting and high-cost patient identification demonstrate that large-scale pretraining captures complex healthcare dynamics that are not easily represented in conventional machine learning models. This integrated view is particularly important for applications in health system planning and resource allocation.

Importantly, our results also demonstrate the potential of foundation models to transform RWE generation. By incorporating learned representations into propensity score modeling, ReClaim substantially reduces systematic bias in a target trial emulation study. These findings suggest a shift from manually engineered covariates toward data-driven representations that encode latent confounding structures. This representation-based strategy may provide a scalable pathway to improve the robustness and reproducibility of observational studies, addressing longstanding challenges in RWE. More broadly, this work suggests an emerging convergence between representation learning and causal inference, in which foundation models provide shared representations that can be used both for predictive modeling and for improving confounding adjustment in real-world studies.

This work also highlights the importance of scale and post-training in healthcare foundation models. Performance improves monotonically with data and model sizes, and task-specific post-training yields substantial gains across nearly all disease endpoints. Notably, unlike prior large-scale healthcare foundation models such as Delphi [16] and Curiosity [17], which primarily rely on pretraining alone, ReClaim incorporates an explicit post-training stage that adapts representations to downstream clinical objectives. This additional alignment step proves not only highly effective, driving consistent improvements across 97.9% of disease endpoints, but also highly efficient. In particular, post-training is data-efficient, as it delivers large performance gains with substantially less data than pre-training, and it is inference-efficient, as disease probability sampling at test time can be performed directly through instruct tokens, without requiring the costly Monte Carlo sampling over multiple full-sequence generations that is commonly used in prior generative trajectory modeling

approaches. Together, these findings are consistent with scaling laws observed in other domains and suggest that further improvements can be achieved with larger datasets, more diverse populations, and more advanced adaptation strategies.

Although scaling and post-training remain promising paths to improved performance, they also substantially increase training cost. Our results show that careful tokenized sequence design, tailored to the structure of the source data, can offer a more parsimonious route to performance gains. Three design choices were particularly important. First, claims-based RWD are sparse and event-driven, making temporal encoding essential. We used anchor tokens to provide absolute temporal reference points and encode elapsed time during periods without observed healthcare events, allowing the model to learn evolving risk and utilization patterns during both event-rich and clinically silent intervals. This design is conceptually aligned with Delphi, which introduced “no-event” tokens to break up long event-free intervals [16]. Second, given the administrative noise, heterogeneous coding and imperfect temporal precision of claims data, monthly aggregation provided a practical balance between noise reduction and temporal fidelity in our setting, suggesting that the optimal granularity for longitudinal foundation models is likely data- and task-specific and should be explored before further scaling. Finally, vocabulary design required balancing clinical expressiveness with modeling efficiency. Naively combining ICD-9-CM, ICD-10-CM, NDC and CPT codes in MarketScan yields more than 180,000 tokens, which is inefficient for autoregressive modeling at scale. Rather than excluding long-tail codes to reduce sparsity [17], we used hierarchical standardization and mapping to compress the vocabulary while preserving full traceability to original codes. This substantially reduced vocabulary size at the cost of modestly longer sequences, a trade-off that supported stable training and strong downstream performance.

Several limitations should be considered. First, claims data lack granular clinical information, including laboratory results, imaging findings and narrative notes, which may limit performance for outcomes requiring high-resolution clinical features. Second, claims are generated for billing and reimbursement, and therefore reflect coding practices and financial incentives that may introduce systematic bias. Third, MarketScan represents insured populations and is organized around enrollment episodes rather than complete life courses, so recorded enrollees may not correspond exactly to unique individuals observed over time. Fourth, healthcare expenditure prediction may be sensitive to payer and plan design, particularly negotiated prices and benefit structures. Consequently, predicted expenditure may reflect both underlying health needs and plan-specific patterns of access and reimbursement, limiting transportability to uninsured populations or payer systems with different payment rules. Finally, disease endpoints were defined using ICD-10 groupings to support broad-scale benchmarking and comparability with Delphi, but these groupings may not always align with clinically coherent phenotypes. Alternative definitions, including DRG-based families or phenotype-driven systems such as PheCodes [25], may improve interpretability and downstream clinical utility.

These limitations point to important directions for future research. Integrating claims-based representations with complementary data sources, including EHRs, imaging, and genomics, may enable the development of multimodal healthcare foundation models that capture both breadth and depth of health and healthcare. In addition, further work is needed to understand how foundation model representations can be systematically incorporated into causal inference frameworks and validated across diverse study designs. Advances in model interpretability and fairness will also be critical for safe and equitable deployment in clinical and research settings.

In conclusion, ReClaim demonstrates that large-scale administrative claims data can support the development of generalizable healthcare foundation models with applications spanning disease prediction, expenditure forecasting, and real-world evidence generation. By enabling unified modeling of longitudinal healthcare trajectories at population scale, this framework provides a foundation for a more integrated and data-driven approach to understanding and improving healthcare systems.

## 4 Methods

### 4.1 Training and Evaluation Data

We utilized the Merative MarketScan Research Databases (2008–2024), one of the largest longitudinal U.S. administrative claims resources for healthcare research. The dataset contains person-level claims capturing

**Table 1** | Summary of datasets used for model development and evaluation.

Data source	Role	Dataset	Time range	N
MarketScan Claims	Training	Training corpus	2008 – 2022	118,064,940
	Evaluation	RWE cohort	2008 – 2024	1,000,000
		Predictive benchmark <sup>1</sup>	2008 – 2024	1,000,000
External EHRs	Evaluation	EHRShot <sup>1</sup>	1990 – 2023	5,845
		YNHH <sup>1</sup>	2013 – 2025	113,590

All cohorts include individuals retained after applying predefined inclusion and exclusion criteria and the data processing pipeline.

<sup>1</sup> These cohorts are partitioned into retrospective (data through December 31, 2022) and prospective (outcomes from January 1, 2023 onward using only pre-2023 history) subsets.

healthcare utilization, expenditures, and enrollment across inpatient, outpatient, and outpatient pharmacy settings, comprising approximately 43.8 billion records. This study includes three primary payer databases: Commercial (CCAE), Medicare (MDCR), and Medicaid (MDCD), collectively representing over 200 million unique enrollees (Table A1). After merging the databases and applying inclusion and exclusion criteria (see Supplementary Table A2), followed by the data processing pipeline, a total of 120,064,940 unique enrollees were retained, of whom 54% were female, with an average of 517 tokens and a mean longitudinal duration of 45 months per enrollee. An example of a processed synthetic enrollee is shown in Supplementary Table A3, with detailed processing steps provided in Supplementary Materials A.1.

#### 4.1.1 Training data

**Pre-training cohort** The pre-training corpus comprised 118,064,940 enrollee records, constructed after holding out two non-overlapping evaluation cohorts of 1 million individuals each, with events restricted to those recorded on or before December 31, 2022 (Table 1).

**Post-training cohort** For post-training, we randomly sampled 100,000 enrollee records from a subset of the pre-training data to construct the post-training dataset. We restricted this subset to patient records spanning at least two months. For each sequence, an instruction token was randomly inserted under the constraint that at least two months of historical information preceded the instruction position. All tokens before the instruction token were retained, whereas tokens after the instruction token were restricted to diagnosis tokens corresponding to newly incident disease events. An example of a processed synthetic enrollee in post-training is shown in Supplementary Table A4.

#### 4.1.2 Evaluation data

**In-domain retrospective cohort** A separate held-out cohort of 1 million individuals is reserved for predictive benchmarks, including disease onset prediction and healthcare expenditure forecasting. For retrospective evaluation, assessments are restricted to data observed through December 31, 2022. Task-specific analyses are conducted on enrollees who satisfy the required observation window and follow-up criteria.

**In-domain prospective cohort** The prediction task focuses on disease onsets occurring on or after January 1, 2023, using the same held-out cohort. To ensure a prospective design, model inputs are restricted to each individual’s healthcare history prior to 2023. Outcomes are then ascertained from follow-up data beginning January 1, 2023. Individuals without adequate pre-2023 history or lacking post-2022 follow-up are excluded from this temporal generalization analysis.

**In-domain RWE cohort** One held-out cohort of 1 million individuals is reserved for the downstream RWE case study. Unlike predictive evaluations, the RWE study uses full longitudinal trajectories without temporal partitioning, reflecting broader real-world study settings.

**Out-domain EHR cohort** We incorporate two external EHR-based cohorts for the disease onset prediction task (see Table 1). EHRShot is a public benchmark dataset derived from de-identified structured EHR data from Stanford Medicine [13]. Yale New Haven Hospital (YNHH) is a private hospital-based EHR cohort from a five-hospital academic health system spanning Connecticut and Rhode Island. We include all available individuals from EHRShot given its modest size, and construct the YNHH cohort by randomly sampling from an original population of approximately 3 million individuals. Both datasets are standardized in the Observational Medical Outcomes Partnership Common Data Model (OMOP CDM) and undergo analogous inclusion and exclusion criteria with harmonized preprocessing. Clinical variables are mapped using OHDSI standard vocabularies, and records are transformed into the same longitudinal trajectory schema used for MarketScan, yielding temporally ordered sequences for model inference. For claims-specific variables that are unavailable or differently encoded in EHRs, values are imputed when feasible; expenditure variables, which are not present in EHR data, are assigned the value `MISSING`. As expenditure labels and several claims-specific attributes are unavailable in these datasets, external validation is restricted to disease onset prediction.

## 4.2 Benchmark Tasks

To comprehensively evaluate the ReClaim models on real-world healthcare data, we designed three complementary tasks, following prior work, that reflect key analytical applications of healthcare foundation models: disease onset prediction, healthcare expenditure prediction, and support for comparative effectiveness studies. Baselines include LightGBM [23], a well-established supervised algorithm, and Delphi [16], a recent transformer-based model for longitudinal disease progression and generative simulation.

**Disease onset prediction.** We assess disease onset prediction following the protocol of Delphi [16]. Each patient is represented as a tokenized longitudinal trajectory containing demographics and chronologically ordered diagnosis, procedure, medication, expenditure, and visit-attribute tokens (Table A3). Events are separated by inter-event time tokens (`<ATT-d>`) and year markers (`<NY>`); the age in days associated with each token is reconstructed by accumulating the gap tokens forward from the patient’s birth-year token. For each major ICD-10 endpoint  $k$  in the model vocabulary (e.g., `<DX-MAJOR_E11>` for type 2 diabetes, `<DX-MAJOR_I21>` for acute myocardial infarction, `<DX-MAJOR_C50>` for breast cancer, and `<DX-MAJOR_F32>` for major depressive disorder), we construct a per-disease case-control cohort stratified by age and sex. Prediction times are induced directly from the trajectory rather than selected by an external rule. Specifically, for every event position  $j$  in a patient’s history, we precompute the latest prior position  $\pi(j)$  whose age is at least  $\Delta$  days earlier:

$$\pi(j) = \max\{i < j : \text{age}_i \leq \text{age}_j - \Delta\}.$$

For a case, the outcome event is defined as the patient’s first occurrence of token  $k$ . Prevalent cases are therefore excluded by construction, and only incident first-onset events are counted. The prediction time is set to

$$t_{\text{pred}} = \text{age}_{\pi(j)},$$

where  $j$  denotes the first-occurrence index of token  $k$ . For a control, the patient must have no occurrence of token  $k$  anywhere in the full trajectory. We then sample a prediction time from a non- $k$  token whose induced  $t_{\text{pred}}$  falls within the same age bin and sex stratum as the cases, yielding age- and sex-matched comparisons rather than population-level mixing. Specifically, we define age strata from 20 to 100 years in 10-year intervals.

At inference, the model receives only tokens up to and including  $t_{\text{pred}}$ , followed by the prompt suffix `<NY><INSTRUCT-DX>`. The final-position logit corresponding to vocabulary index  $k$  is used as the risk score. We report AUCs with DeLong variance estimates within each stratum and average performance across strata. Risk is evaluated at four clinically meaningful horizons by varying  $\Delta \in \{1, 6, 12, 60\}$  months, corresponding to  $\Delta \in \{30, 182, 365.25, 1826.25\}$  days. The 1-month setting captures near-term risk relevant to immediate intervention.

A caveat is that case-control assignment is based on exact endpoint tokens. Thus, a patient who is negative for the queried token but positive for a clinically related token is still treated as a control. For example, when evaluating `<DX-MAJOR_R73>` for prediabetes or abnormal glucose, patients carrying `<DX-MAJOR_E11>` for type 2 diabetes are not excluded. The resulting AUC therefore reflects the model’s ability to distinguish coded

prediabetes from all other records, rather than from strictly disease-free controls. The same consideration applies to hierarchical or clinically related pairs such as I21 acute myocardial infarction versus I25 chronic ischemic heart disease, or C50 breast cancer versus Z80.3 family history of breast cancer and D05 carcinoma in situ of breast. For endpoints where such hierarchy is material, AUCs should be interpreted as discrimination of diagnoses as recorded in claims rather than as a pure disease-incidence model. We follow the Delphi convention of evaluating each endpoint identically and leave related-token exclusion to a follow-up sensitivity analysis.

**Healthcare expenditure prediction** We formulate next-year healthcare expenditure prediction as estimating an enrollee’s total gross payments to all providers in the subsequent calendar year, following prior work [26]. For each enrollee, an eligible prediction point with at least one year of prior history and one year of follow-up partitions the longitudinal sequence into a preceding context segment and a subsequent outcome segment; the former serves as model input, while the latter is used to derive the target, defined as total healthcare expenditure over the following calendar year. Model performance is evaluated under both continuous regression and classification settings, with thresholds in Supplementary Table A10 informed by the 2022 MEPS report [27]. For classification, we consider (1) three-level expenditure stratification using cutoffs of \$1,500 (approximately the 50th percentile) and \$15,000 (approximately the 90th percentile), and (2) identification of HNHC patients using a binary threshold of \$30,000 (approximately the 95th percentile). As in the disease onset prediction task, we report both final internal performance on a disjoint held-out test cohort of 1 million patients and assess temporal generalization on a prospective temporal evaluation built from events occurring after January 1, 2023, where only pre-2023 history is available as input.

We evaluate pretrained ReClaim models across all healthcare expenditure prediction tasks. For each prediction instance, the model is prompted with the input sequence corresponding to the historical context segment. Using the default sampling configuration (temperature = 1, top- $p$  = 1), the model probabilistically generates 20 simulated future trajectories [17]. From each simulated trajectory, cost tokens corresponding to the subsequent year are extracted and aggregated to estimate annual healthcare expenditures.

**Support for real-world evidence analyses** The validity of observational RWE studies is often threatened by systematic error arising from selection bias and confounding. Propensity score methods are widely used to address measured confounding by balancing observed covariates between treatment groups. Negative control outcomes (NCOs), defined as outcomes with no plausible causal relationship with the treatments under study but expected to share similar sources of bias with the outcomes of interest, provide empirical anchors for quantifying and calibrating residual systematic bias [28, 29, 30]. To assess whether ReClaim-derived representations improve confounding adjustment in observational RWE analyses, we conducted an embedding-augmented target trial emulation adapted from a recent study of the association between GLP-1 receptor agonist use and psychiatric outcomes [31]. We used the dedicated held-out RWE cohort to compare three antidiabetic drug classes: glucagon-like peptide-1 receptor agonists (GLP-1 RAs), sodium–glucose cotransporter-2 inhibitors (SGLT-2is) and dipeptidyl peptidase-4 inhibitors (DPP-4is). Key definitions, including the primary psychiatric outcomes and curated negative control outcomes (NCOs), are provided in Supplementary Tables A11, A12 and A13. Outcomes with a prevalence below 0.5% in the analytic cohort were excluded.

For each pairwise treatment comparison, propensity scores were estimated using LASSO-penalized logistic regression under three configurations: traditional covariates alone, including age, sex, medical conditions and medication classes from the baseline period, and traditional covariates augmented with either Delphi or ReClaim-L embeddings. For embedding-augmented analyses, each individual’s pre-index sequence was encoded into a representation vector and appended to the covariate set. Individuals were then matched 1:1 using nearest-neighbour propensity score matching. Within matched cohorts, treatment effects for primary and negative control outcomes (NCOs) were estimated using Poisson regression with a log link and Huber–White robust standard errors, yielding rate ratios. NCO estimates were used to fit an empirical null distribution, with residual bias summarized by the expected absolute systematic error (EASE) and used to calibrate effect estimates.

### 4.3 Model Pre-training and Post-training

ReClaim uses decoder-only Transformer architectures following Qwen3 dense model [32], but all model weights are learned *de novo* rather than initialized from any released Qwen3 checkpoint. All variants operate on the same custom tokenizer and vocabulary. Given an input token sequence, the model computes contextual representations through stacked Transformer blocks with causal self-attention and predicts the next token with a linear output layer tied to the input embedding matrix.

We trained three model scales within this shared architectural family: **140M**, **700M** and **1.7B** parameters (see Supplementary Table A14 for details). The three variants differ primarily in depth and width while retaining the same overall architecture and vocabulary, so observed performance differences predominantly reflect model capacity rather than changes in tokenization or model design.

**Large-scale pre-training** We first pre-train each model with a standard **next-token prediction** objective on tokenized patient trajectories under our custom vocabulary. Given a tokenized sequence  $x_{1:T}$ , we maximize

$$\sum_{t=1}^T \log p_{\theta}(x_t | x_{<t}), \tag{1}$$

which is implemented as cross-entropy between the predicted distribution and the ground-truth next token with a causal attention mask. In addition to cross-entropy loss  $\mathcal{L}_{\text{CE}}$ , we apply a  $z$ -loss regularization term that penalizes the squared log-partition value computed from the logits. Let  $\mathbf{s}_t \in \mathbb{R}^{|\mathcal{V}|}$  denote the logits at position  $t$  over the vocabulary  $\mathcal{V}$ , and define

$$Z_t = \sum_{v \in \mathcal{V}} \exp(s_{t,v}). \tag{2}$$

We then add

$$\mathcal{L}_z = \lambda \cdot \mathbb{E}[(\log Z_t)^2], \quad \lambda = 10^{-4}, \tag{3}$$

and the total pre-training loss is

$$\mathcal{L} = \mathcal{L}_{\text{CE}} + \mathcal{L}_z. \tag{4}$$

This regularizer discourages excessive logit magnitude and global logit drift, which are only weakly constrained by cross-entropy alone. In practice, it improved numerical stability under large-scale training, reduced loss spikes and yielded more stable logit scales during optimization.

**Task-specific post-training** Because pre-training optimizes general sequence modeling rather than endpoint-specific risk prediction, we performed a single task-specific post-training stage for **disease onset prediction**. To construct the post-training data, we transformed each patient trajectory into a prompt–response pair derived from the original longitudinal record. For each sequence, we randomly selected a position and inserted an instruction token at that point. The sequence preceding the instruction token was used as the prompt. In the subsequent segment, we retained only diagnosis tokens corresponding to newly incident disease events, and these tokens formed the response. This construction trains the model to map historical longitudinal context to incident disease outputs while suppressing unrelated future tokens. We post-train the pre-trained model on 100,000 such pairs using causal next-token prediction on the concatenated prompt–response sequence, while masking the loss on prompt tokens so that optimization is confined to the response region. Given an instruction prompt  $p$  and a reference response  $y_{1:K}$ , we optimize

$$\sum_{k=1}^K \log p_{\theta}(y_k | p, y_{<k}). \tag{5}$$

This stage aligns the pre-trained model with disease onset prediction by restricting supervision to the response region, so that the model learns to predict newly incident diseases from the preceding longitudinal context while keeping the tokenizer and vocabulary unchanged from pre-training.

## 4.4 Compared Baseline

**Disease-specific LightGBM** We use LightGBM [23] as a strong tabular baseline for both disease prediction and healthcare expenditure prediction. For disease prediction, LightGBM is trained on word-count features extracted from each patient’s historical record over the observation window, together with demographic variables. This bag-of-words representation preserves event occurrence and frequency information but discards event order and temporality. For healthcare expenditure prediction, we follow prior work [26] and construct a LightGBM regressor using features derived from the preceding context segment, including demographics, diagnosis codes, drug codes, and prior-year total expenditure, where available. Diagnosis and medication codes are likewise represented as bag-of-words frequency counts over the observation window. For both tasks, model development is performed on a randomly sampled subset of 5 million individuals from the training corpus, consistent with Curiosity [17].

**Pre-trained Delphi** We followed the publicly released Delphi code base [16] and used the released model and default settings for training. Delphi is trained on the full available MarketScan corpus. We retain only the demographic tokens and disease-target events required by the public implementation when constructing Delphi inputs. Delphi is then evaluated on the same retrospective held-out, prospective temporal, and external disease endpoint sets whenever compatible labels are available.

## References

- [1] Rachel E. Sherman, Steven A. Anderson, Gerald J. Dal Pan, Gerry W. Gray, Thomas Gross, Nina L. Hunter, Lisa LaVange, Danica Marinac-Dabic, Peter W. Marks, Melissa A. Robb, Jeffrey Shuren, Robert Temple, Janet Woodcock, Lilly Q. Yue, and Robert M. Califf. Real-world evidence—what is it and what can it tell us? *New England Journal of Medicine*, 375(23):2293–2297, 2016.
- [2] Fang Liu and Demosthenes Panagiotakos. Real-world data: a brief review of the methods, applications, challenges and opportunities. *BMC Medical Research Methodology*, 22(1):287, 2022.
- [3] Miguel A. Hernán and James M. Robins. Using big data to emulate a target trial when a randomized trial is not available. *American Journal of Epidemiology*, 183(8):758–764, 2016.
- [4] John Concato and Jacqueline Corrigan-Curay. Real-world evidence—where are we now? *New England Journal of Medicine*, 386(18):1680–1682, 2022.
- [5] U.S. Food and Drug Administration. Real-world data: Assessing electronic health records and medical claims data to support regulatory decision-making for drug and biological products. Guidance for industry, U.S. Food and Drug Administration, 2024. Issued July 2024.
- [6] Yikuan Li, Shishir Rao, Jose Roberto Ayala Solares, Abdelaali Hassaine, Dexter Canoy, Yuan Zhu, Kazem Rahimi, and Gholamreza Salimi-Khorshidi. BEHRT: Transformer for electronic health records. *Scientific Reports*, 10(1):7155, 2020.
- [7] Laila Rasmy, Yang Xiang, Ziqian Xie, Cui Tao, and Degui Zhi. Med-BERT: pretrained contextualized embeddings on large-scale structured electronic health records for disease prediction. *npj Digital Medicine*, 4(1):86, 2021.
- [8] Ethan Steinberg, Ken Jung, Jason A. Fries, Conor K. Corbin, Stephen R. Pfohl, and Nigam H. Shah. Language models are an effective representation learning technique for electronic health record data. *Journal of Biomedical Informatics*, 113:103637, 2021.
- [9] Zhichao Yang, Avijit Mitra, Weisong Liu, Dan Berlowitz, and Hong Yu. Transformehr: transformer-based encoder-decoder generative model to enhance prediction of disease outcomes using electronic health records. *Nature Communications*, 14:7857, 2023.
- [10] Ethan Steinberg, Jason Fries, Yizhe Xu, and Nigam H. Shah. Motor: A time-to-event foundation model for structured medical records. *arXiv preprint arXiv:2301.03150*, 2023.

- [11] Chao Pang, Xinzhuo Jiang, Nishanth Parameshwar Pavinkurve, Krishna S. Kalluri, Elise L. Minto, Jason Patterson, Linying Zhang, George Hripcsak, Gamze Gürsoy, Noémie Elhadad, and Karthik Natarajan. Cehr-gpt: Generating electronic health records with chronological patient timelines. *arXiv preprint arXiv:2402.04400*, 2024.
- [12] Matthew B. A. McDermott, Bret Nestor, Peniel Argaw, and Isaac Kohane. Event stream gpt: A data pre-processing and modeling library for generative, pre-trained transformers over continuous-time sequences of complex events. *arXiv preprint arXiv:2306.11547*, 2023.
- [13] Michael Wornow, Rahul Thapa, Ethan Steinberg, Jason Fries, and Nigam Shah. EHRSHOT: An EHR benchmark for few-shot evaluation of foundation models. In *Advances in Neural Information Processing Systems*, volume 36, pages 67125–67137, 2023. Datasets and Benchmarks Track.
- [14] Zeljko Kraljevic, Dan Bean, Anthony Shek, Rebecca Bendayan, Harry Hemingway, Joshua Au Yeung, Alexander Deng, Alfred Balston, Jack Ross, Esther Idowu, James T. Teo, and Richard J. B. Dobson. Foresight—a generative pretrained transformer for modelling of patient timelines using electronic health records: a retrospective modelling study. *The Lancet Digital Health*, 6(4):e281–e290, 2024.
- [15] Pawel Renc, Yugang Jia, Anthony E Samir, Jaroslaw Was, Quanzheng Li, David W Bates, and Arkadiusz Sitek. Zero shot health trajectory prediction using transformer. *npj Digital Medicine*, 7(1):256, 2024.
- [16] Artem Shmatko, Alexander Wolfgang Jung, Kumar Gaurav, Søren Brunak, Laust Hvas Mortensen, Ewan Birney, Tom Fitzgerald, and Moritz Gerstung. Learning the natural history of human disease with generative transformers. *Nature*, 647(8088):248–256, 2025.
- [17] Shane Waxler, Paul Blazek, Davis White, Daniel Sneider, Kevin Chung, Mani Nagarathnam, Patrick Williams, Hank Voeller, Karen Wong, Matthew Swanhorst, et al. Generative medical event models improve with scale. *arXiv preprint arXiv:2508.12104*, 2025.
- [18] Sheng Zhang, Qin Liu, Naoto Usuyama, Cliff Wong, Tristan Naumann, and Hoifung Poon. Exploring scaling laws for ehr foundation models. *arXiv preprint arXiv:2505.22964*, 2025.
- [19] Michael Wornow, Yizhe Xu, Rahul Thapa, Birju Patel, Ethan Steinberg, Scott Fleming, Michael A. Pfeffer, Jason Fries, and Nigam H. Shah. The shaky foundations of large language models and foundation models for electronic health records. *npj Digital Medicine*, 6:135, 2023.
- [20] Xianlong Zeng, Simon L. Linwood, and Chang Liu. Pretrained transformer framework on pediatric claims data for population specific tasks. *Scientific Reports*, 12:3651, 2022.
- [21] Ricky Sahu, Eric Marriott, Ethan Siegel, David Wagner, Flore Uzan, Troy Yang, and Asim Javed. Introducing the large medical model: State of the art healthcare cost and risk prediction with transformers trained on patient event sequences. *arXiv preprint arXiv:2409.13000*, 2024.
- [22] Chao Pang, Vincent Jeanselme, Young Sang Choi, Xinzhuo Jiang, Zilin Jing, Aparajita Kashyap, Yuta Kobayashi, Yanwei Li, Florent Pollet, Karthik Natarajan, and Shalmali Joshi. Fomoh: A clinically meaningful foundation model evaluation for structured electronic health records. *arXiv preprint arXiv:2505.16941*, 2025.
- [23] Guolin Ke, Qi Meng, Thomas Finley, Taifeng Wang, Wei Chen, Weidong Ma, Qiwei Ye, and Tie-Yan Liu. Lightgbm: A highly efficient gradient boosting decision tree. In *Advances in Neural Information Processing Systems 30*, 2017.
- [24] Stéphanie Nguengang Wakap, Deborah M. Lambert, Annie Olry, Charlotte Rodwell, Charlotte Gueydan, Valérie Lanneau, Daniel Murphy, Yann Le Cam, and Ana Rath. Estimating cumulative point prevalence of rare diseases: analysis of the orphanet database. *European Journal of Human Genetics*, 28:165–173, 2020.

- [25] Wei-Qi Wei, Lisa A. Bastarache, Robert J. Carroll, Joy E. Marlo, Travis J. Osterman, Eric R. Gamazon, Nancy J. Cox, Dan M. Roden, and Joshua C. Denny. Evaluating phecodes, clinical classification software, and icd-9-cm codes for phenome-wide association studies in the electronic health record. *PLOS ONE*, 12(7):e0175508, 2017.
- [26] Itsuki Osawa, Tadahiro Goto, Yuji Yamamoto, and Yusuke Tsugawa. Machine-learning-based prediction models for high-need high-cost patients using nationwide clinical and claims data. *NPJ digital medicine*, 3(1):148, 2020.
- [27] Adriana Hernandez-Viver and Emily M. Mitchell. Concentration of healthcare expenditures and selected characteristics of persons with high expenses, u.s. civilian noninstitutionalized population, 2018–2022. Statistical Brief 560, Agency for Healthcare Research and Quality, Rockville, MD, 2025. AHRQ Publication No. 25-0017-3-EF.
- [28] Marc Lipsitch, Eric Tchetgen Tchetgen, and Ted Cohen. Negative controls: a tool for detecting confounding and bias in observational studies. *Epidemiology*, 21(3):383–388, 2010.
- [29] Martijn J Schuemie, Patrick B Ryan, William DuMouchel, Marc A Suchard, and David Madigan. Interpreting observational studies: why empirical calibration is needed to correct p-values. *Statistics in medicine*, 33(2):209–218, 2014.
- [30] Mitchell M Conover, Patrick B Ryan, Yong Chen, Marc A Suchard, George Hripcsak, and Martijn J Schuemie. Objective study validity diagnostics: a framework requiring pre-specified, empirical verification to increase trust in the reliability of real-world evidence. *Journal of the American Medical Informatics Association*, 32(3):518–525, 2025.
- [31] Huilin Tang, Yiwen Lu, Bingyu Zhang, Dazheng Zhang, Ting Zhou, Jiajie Chen, Ying Lu, Tianchu Lyu, Kai Zheng, and Yong Chen. Association of glp-1 receptor agonist use with psychiatric outcomes in adults with type 2 diabetes: a target trial emulation. *Diabetes Research and Clinical Practice*, page 113038, 2025.
- [32] Qwen Team. Qwen3 technical report. *arXiv preprint arXiv:2505.09388*, 2025.

## A Supplementary Materials

**Table A1** | Overview of the Merative MarketScan Research Databases.

Database	Description	Time range	N
CCAЕ	Commercial claims for employer-sponsored populations, including employees, early (non-Medicare) retirees, COBRA continuees, and dependents.	Jan 2008 – Sep 2024	165,720,281
MDCR	Medicare claims for Medicare-eligible employees and retirees and their dependents in employer-sponsored supplemental and Medicare Advantage plans; predominantly fee-for-service data.	Jan 2009 – Sep 2024	11,091,216
MDCD	Multi-state Medicaid claims capturing healthcare utilization for individuals enrolled in Medicaid programs across participating states, including fee-for-service and managed care plans.	Jan 2009 – Jun 2024	28,787,210

**Table A2** | Standardized Inclusion and Exclusion Criteria Applied Across Payer Databases

Criterion	Description
Database linkage	CCAЕ and MDCR databases were merged using shared enrollee identifiers for individuals linkable across payer systems. As a subset of individuals are linkable between CCAЕ and MDCR via shared enrollee identifiers, whereas MDCD identifiers are unique and non-overlapping across databases.
Valid enrollee identifier	Consistent enrollee identifier required to enable longitudinal linkage of claims
Prescription drug coverage	Enrollment periods with documented prescription drug coverage required to ensure complete pharmacy claims for medication exposure assessment
Minimum enrollment duration	$\geq 180$ cumulative days of enrollment required to provide sufficient observation time
Minimum claims span	$\geq 30$ -day span between first and last observed claims to exclude transient or fragmented records
Age restriction	Age at first observed event restricted to 10–110 years to represent realistic clinical populations
Dual-eligible exclusion	Medicare dual-eligible beneficiaries excluded from the MDCD database to prevent cross-database linkage and data leakage

## A.1 Data Processing

To ensure comprehensive representation and compatibility across the three MarketScan payer databases, we selected a harmonized set of demographic, enrollment, clinical, and financial variables. For demographic information, we collected biological sex and year of birth, as MarketScan does not provide additional demographic attributes such as race or ethnicity. For enrollment information, we extracted payer type, insurance plan type, indicator of capitated coverage, and state-level geographic location. Clinical information was collected according to claim type, including outpatient pharmaceutical, outpatient visit, and inpatient admission claims. Pharmacy claims included National Drug Codes (NDCs). Outpatient claims included diagnosis codes from the International Classification of Diseases, Tenth Revision, Clinical Modification (ICD-10-CM), and procedure codes primarily from Current Procedural Terminology, Fourth Edition (CPT-4). Inpatient admission records included diagnosis codes, procedure codes primarily based on the International Classification of Diseases, Tenth Revision, Procedure Coding System (ICD-10-PCS), length of stay, and discharge status. For financial variables, we used the gross payment amount associated with each claim.

We adapted the tokenization framework proposed in prior work [15, 16] to transform each enrollee’s longitudinal claims history into a structured, chronologically ordered token sequence suitable for autoregressive modeling. Missing or unavailable values across all variables were standardized and assigned the value `MISSING`. Tokens in the resulting sequence are categorized into two types depending on whether they carry explicit temporal information: static tokens and temporal tokens aggregated at a specified temporal resolution.

**Temporal resolution and data aggregation** Although the IBM MarketScan Research Databases record claims at daily resolution, latency and irregular reporting delays can distort the true temporal ordering of clinical events. Aggregation to a coarser temporal scale mitigates this noise; among daily, weekly, and monthly granularities, monthly aggregation yielded the best downstream performance in ablation studies. Accordingly, temporal event tokens were grouped by calendar month within each claim type. Within each month, tokens were aggregated either by summation or by deduplication based on first occurrence, then ordered according to their original finer-resolution timestamps (dates) when available. Finally, tokens occurring at the same timestamp were deterministically ordered according to the rules illustrated in Supplementary Table A7.

**Static tokens** Static tokens are time-invariant and positioned independently of temporal events. The sex token is treated as static and positioned at the start of the sequence. Additional static tokens include special instruction tokens that are manually inserted to signal the initiation of post-training tasks.

**Enrollment token** Each enrollment episode is represented by an enrollment-start token group and a corresponding enrollment-end token. The start group captures key attributes of the healthcare plan, consisting of an enrollment-start flag followed by tokens encoding plan type, capitated coverage status, and geographic location, all aligned to the calendar month of the enrollment start date. The enrollment-end token is aligned to the calendar month of the enrollment end date and marks the termination of the episode.

**Clinical tokens** MarketScan encodes clinical information using heterogeneous coding systems that vary across care settings and time periods. To enable unified representation learning and control vocabulary size, each code domain was standardized while preserving high mapping coverage and minimizing information loss. Diagnosis codes recorded in ICD-9-CM before 2015 were mapped to ICD-10-CM using the Centers for Medicare & Medicaid Services General Equivalence Mappings. ICD-10-CM codes were then decomposed into up to three hierarchical components, major, minor and suffix, according to code granularity. Procedure codes from CPT-4, ICD-9 Procedure Coding System (ICD-9-Proc) and ICD-10-PCS were harmonized to Systematized Nomenclature of Medicine Clinical Terms (SNOMED CT) concepts using the Observational Health Data Sciences and Informatics Athena standard vocabulary (v20250827), with CPT-4 codes retained only when no SNOMED CT mapping was available, as this approach provides more consistent cross-mapping to ICD-10-PCS while yielding a smaller effective vocabulary. Drug product codes recorded as 11-digit NDC values were first mapped to RxNorm drug-level concepts and then collapsed to RxNorm active ingredients. Multi-target mappings (for example, one-to-many SNOMED CT procedure mappings or combination drugs) were enclosed by special combination start and end tokens to preserve atomic groupings. Tokens in each atomic group are sorted alphabetically to form a unique, canonical representation, enabling one-to-one mapping to

the original code. Within each monthly aggregated encounter, repeated occurrences of the same standardized clinical code are collapsed by retaining the earliest instance, and the resulting unique codes are ordered by their original dates. Principal diagnosis and procedure codes are indicated by a preceding principal marker token, as are secondary diagnosis and procedure codes. Codes that fail to map to the standardized vocabulary are assigned the value `NOMAP`.

**Cost token** We used gross payment as the measure of healthcare expenditure in foundation model pretraining. Gross payment reflects the amount eligible for payment after applying pricing rules, such as fee schedules and discounts, but before deductibles, copayments and coordination of benefits. It therefore provides a stable estimate of expenditure magnitude that is closely tied to the recorded clinical event and less sensitive to patient-specific or plan-specific payment variation, which can differ substantially across insurance benefit designs and cost sharing arrangements. Incorporating this expenditure signal into longitudinal token sequences requires a representation that can accommodate the wide dynamic range of healthcare costs, which span several orders of magnitude from small pharmacy payments to high-cost inpatient stays. We therefore discretized expenditure into tokens that capture approximate magnitude. For each monthly timestep, gross payment within the same claim type were summed, rounded to one significant digit using standard half-up rounding, and encoded as a two-digit scientific-notation-style value, with the first digit representing the leading significant digit and the second representing the order of magnitude. For example, \$2,400 is rounded to 2,000 and encoded as 23, corresponding to  $2 \times 10^3$ , while \$859 is rounded to 900 and encoded as 92, corresponding to  $9 \times 10^2$ ; zero or negative values are encoded as 0. This logarithmic discretization yields a compact vocabulary of 100 cost tokens covering values up to  $9 \times 10^9$ . It preserves relative magnitude while assigning finer resolution to lower-cost events and coarser resolution to high-cost events, where order-of-magnitude differences are more informative.

**Interval and anchor tokens** Temporal information is encoded through a combination of artificial time tokens and anchor tokens. Artificial time tokens  $\langle \text{ATT-}N \rangle$  are inserted between consecutive monthly event-token groups, where  $N$  denotes the number of elapsed months. To bound  $N \in 0, 1, \dots, 12$  and maintain alignment with calendar time, a *New Year* token  $\langle \text{NY} \rangle$  is introduced at the first month of each calendar year, serving as a recurring calendar anchor. Additional anchor tokens provide absolute reference points: a year-of-birth token placed at the first month of the birth year, and an age token encoding the enrollee’s age at their first observed claim, assigned to the first month of that year. Together, these tokens encode time in a relative form while preserving the ability to recover absolute calendar time.

**Vocabulary construction** To control vocabulary size while maintaining adequate coverage, clinical code tokens were populated only from codes observed in the training data rather than from the full set of theoretically possible codes in the original coding systems. The vocabulary was further substantially compressed through the standardized mapping procedures described in the Clinical tokens paragraph above. For other token categories, the vocabulary was constructed as the union of values observed in the training data and all allowable values exhaustively defined in the MarketScan data dictionary. A summary of the resulting vocabulary is provided in Supplementary Table A8.

**Sequence assembly** We organize temporal token groups into six major event categories that collectively define each enrollee’s longitudinal healthcare trajectory: (1) anchor events, including age tokens that encode temporal context and enable alignment to calendar time; (2) enrollment start, capturing plan attributes and coverage characteristics; (3) outpatient visits, including diagnosis and procedure information; (4) outpatient pharmaceutical visits, including prescription records; (5) inpatient admissions, including diagnosis, procedures, discharge status and length of stay; and (6) enrollment end. For each individual, tokens are assembled into a single longitudinal sequence that begins with static demographic tokens, such as sex, followed by temporally ordered predefined events aggregated at monthly resolution. Consecutive monthly events are separated by artificial time tokens encoding the number of elapsed months to the next observed event. Within each month, events and their associated tokens are deterministically ordered according to the hierarchy defined in Supplementary Table A7, ensuring a unique and reproducible sequence representation. This assembly yields a compact, information-complete representation that preserves temporal structure and healthcare event heterogeneity in a form suitable for autoregressive modeling. A synthetic example of the resulting token sequence is shown in Table A3, with a detailed step-by-step decoding provided in Supplementary Table A9 to

**Table A3 | Example token sequence for a synthetic enrollee.** Tokenized representation of a synthetic MarketScan enrollee’s longitudinal healthcare trajectory, illustrating the output of our data-processing and customized tokenization pipeline. Tokens appear verbatim in chronological order.

```

<eos> <SEX-1> <DOBYR-1974> <AGE-44> <ATT-0> <ERLST-CCAE> <PLANTYP-6> <CAP-0> <EGEOLC-04> <ATT-12> <NY> <ATT-12> <NY> <ATT-10>
<VT-outpatient> <DX-PRINCIPAL> <DX-MAJOR_R07> <DX-MINOR_9> <DX-MAJOR_E11> <DX-MINOR_9> <PROC-PRINCIPAL> <PROC-COMBSTART>
<PROC-268400002> <PROC-29303009> <PROC-308561006> <PROC-COMBEND> <PROC-165102003> <PROC-16254007> <PROC-COMBSTART>
<PROC-408254005> <PROC-43396009> <PROC-COMBEND> <PROC-CPT499214> <COST-32> <ATT-0> <VT-pharmacy> <RX-6809> <COST-51> <ATT-2>
<NY> <ATT-5> <VT-outpatient> <DX-PRINCIPAL> <DX-MAJOR_I10> <PROC-PRINCIPAL> <PROC-165102003> <PROC-16254007> <PROC-COMBSTART>
<PROC-408254005> <PROC-43396009> <PROC-COMBEND> <PROC-45896001> <PROC-34608000> <PROC-CPT499213> <COST-12> <ATT-0>
<VT-pharmacy> <RX-18867> <RX-5487> <COST-51> <ATT-1> <VT-outpatient> <DX-PRINCIPAL> <DX-MAJOR_E11> <DX-MINOR_9> <DX-MAJOR_E78>
<DX-MINOR_2> <PROC-PRINCIPAL> <PROC-165102003> <PROC-16254007> <PROC-COMBSTART> <PROC-408254005> <PROC-43396009> <PROC-COMBEND>
<PROC-63476009> <PROC-45896001> <PROC-34608000> <COST-22> <ATT-0> <VT-pharmacy> <RX-1991302> <RX-4018> <COST-23> <ATT-6> <NY>
<ATT-3> <VT-inpatient> <DX-PRINCIPAL> <DX-MAJOR_R11> <DX-MINOR_2> <DX-SECONDARY> <DX-MAJOR_R10> <DX-MINOR_9> <DX-MAJOR_R13>
<DX-MINOR_0> <DX-MAJOR_R13> <DX-MINOR_10> <DX-MAJOR_Z98> <DX-MINOR_84> <PROC-SECONDARY> <PROC-168702005> <PROC-241157000>
<PROC-COMBSTART> <PROC-315639002> <PROC-86181006> <PROC-COMBEND> <DS-MISSING> <LS-0> <COST-43> <ATT-9> <NY> <ATT-3>
<VT-outpatient> <DX-PRINCIPAL> <DX-MAJOR_E11> <DX-MINOR_9> <PROC-PRINCIPAL> <PROC-165102003> <PROC-16254007> <PROC-COMBSTART>
<PROC-408254005> <PROC-43396009> <PROC-COMBEND> <PROC-45896001> <PROC-COMBSTART> <PROC-117356000> <PROC-43789009>
<PROC-COMBEND> <PROC-104154005> <PROC-CPT499214> <COST-22> <ATT-8> <ERLED-CCAE> <eos>

```

illustrate how individual tokens map back to the original records.

**Table A4 | Example token sequence for a synthetic enrollee in disease onset prediction post-training.** During disease onset prediction post-training, an <INSTRUCT-DX> token was randomly inserted into the sequence, and diseases newly occurring after this instruction token were defined as the prediction targets.

```

<eos> <SEX-1> <DOBYR-1974> <AGE-44> <ATT-0> <ERLST-CCAE> <PLANTYP-6> <CAP-0> <EGEOLC-04> <ATT-12> <NY> <ATT-12> <NY> <ATT-10>
<VT-outpatient> <DX-PRINCIPAL> <DX-MAJOR_R07> <DX-MINOR_9> <DX-MAJOR_E11> <DX-MINOR_9> <PROC-PRINCIPAL> <PROC-COMBSTART>
<PROC-268400002> <PROC-29303009> <PROC-308561006> <PROC-COMBEND> <PROC-165102003> <PROC-16254007> <PROC-COMBSTART>
<PROC-408254005> <PROC-43396009> <PROC-COMBEND> <PROC-CPT499214> <COST-32> <ATT-0> <VT-pharmacy> <RX-6809> <COST-51> <ATT-2>
<NY> <ATT-5> <VT-outpatient> <DX-PRINCIPAL> <DX-MAJOR_I10> <PROC-PRINCIPAL> <PROC-165102003> <PROC-16254007> <PROC-COMBSTART>
<PROC-408254005> <PROC-43396009> <PROC-COMBEND> <PROC-45896001> <PROC-34608000> <PROC-CPT499213> <COST-12> <ATT-0>
<VT-pharmacy> <RX-18867> <RX-5487> <COST-51> <INSTRUCT-DX> <DX-MAJOR_E11> <DX-MAJOR_E78> <DX-MAJOR_R11> <DX-MAJOR_R10>
<DX-MAJOR_R13> <DX-MAJOR_R13> <DX-MAJOR_Z98> <DX-MAJOR_E11> <eos>

```

**Table A5 | Per-disease prevalence (per 1,000,000) across MarketScan, EHRShot, and YNHH cohorts.** Comparisons are restricted to 1,013 disease endpoints common to all three cohorts. Cohort sizes ( $N$ ) refer to the unique individuals available for evaluation. Statistical comparisons are paired two-sided Wilcoxon signed-rank tests of per-disease prevalence against MarketScan.

Cohort	Median (IQR) per 1M	Median ratio vs MarketScan	$P$ vs MarketScan
MarketScan ( $N = 1,000,000$ )	1,359 (240–5,318)	1.00	—
EHRShot ( $N = 5,845$ )	3,764 (855–14,029)	$2.95 \times$	$5.5 \times 10^{-114}$
YNHH ( $N = 113,590$ )	1,963 (370–8,029)	$1.49 \times$	$2.9 \times 10^{-41}$

EHRShot prevalence exceeded MarketScan in 88.8% of overlapping diseases (900/1,013), with  $\geq 2\times$  in 665 and  $\geq 5\times$  in 325; YNHH exceeded MarketScan in 73.0% (739/1,013). Spearman rank correlation: MarketScan vs EHRShot  $\rho = 0.875$ , MarketScan vs YNHH  $\rho = 0.930$ , indicating that endpoint ranking by prevalence is preserved despite large absolute differences. Differences across cohorts reflect distinct sampling frames: MarketScan covers commercially insured individuals (working-age, healthier baseline), whereas EHRShot and YNHH represent hospital-encountered populations enriched for clinically active patients.

**Table A6 | Distribution of overlapping diseases by prevalence band (per 1,000,000) in each cohort.** Each cell shows the disease count followed by the percentage of the 1,013 overlapping endpoints that fall within the indicated band.

Prevalence band (per 1M)	MarketScan	EHRShot	YNHH
< 100	123 (12.1%)	0 (0.0%)	96 (9.5%)
100–499	226 (22.3%)	133 (13.1%)	202 (19.9%)
500–999	117 (11.5%)	130 (12.8%)	110 (10.9%)
1,000–4,999	284 (28.0%)	307 (30.3%)	264 (26.1%)
5,000–9,999	89 (8.8%)	122 (12.0%)	120 (11.8%)
≥ 10,000	174 (17.2%)	321 (31.7%)	221 (21.8%)

The distribution of overlapping diseases shifts toward higher prevalence bands from MarketScan to YNHH to EHRShot. Endpoints with prevalence below 500 per 1,000,000 account for 34.5% of MarketScan diseases, 29.4% of YNHH and only 13.1% of EHRShot, whereas endpoints with prevalence at or above 10,000 per 1,000,000 comprise 17.2% (MarketScan), 21.8% (YNHH) and 31.7% (EHRShot).

**Table A7** | Deterministic ordering of simultaneous tokens within the same monthly timestamp. Token ordering follows a two-level hierarchy: (i) event-level order and (ii) within-event token ordering.

Event type	Event order	Within-event token order
Anchor	1	AGE NY
Enrollment start	2	ERLST PLANTYP CAP EGEoloc
Outpatient visit	3	VT DX-PRINCIPAL DX codes (principal) DX-SECONDARY DX codes (secondary) PROC-PRINCIPAL PROC codes (principal) PROC-SECONDARY PROC codes (secondary) COST
Pharmacy visit	4	VT RX COST
Inpatient admission	5	VT DX-PRINCIPAL DX codes (principal) DX-SECONDARY DX codes (secondary) PROC-PRINCIPAL PROC codes (principal) PROC-SECONDARY PROC codes (secondary) DS LS COST
Enrollment end	6	ERLED

**Notes:** Event groups occurring within the same monthly timestamp are first ordered according to the event-level order. Within each event, tokens follow a fixed, category-specific sequence listed from top to bottom. For diagnosis (DX) and procedure (PROC) tokens, principal and secondary markers define sub-ordering, and individual codes within each subgroup are ordered by their original dates, after first-occurrence deduplication.

Table A8 | Vocabulary summary.

Type <sup>1</sup>	Category	Token Name	Description	Token Example	Unique Values	Frequency (Million)
Static	Demographic	SEX	Enrollee’s sex	<SEX-1>	3	120
	Instruct	INSTRUCT	Instruction for post-train task	<INSTRUCT-DX>	2	
Temporal	Time	DOBYR	Birth year	<DOBYR-1985>	116	120
		AGE	Age at first event year	<AGE-45>	101	120
		NY	New-year marker	<NY>	1	379
		ATT	Months to next encounter	<ATT-5>	13	4,467
	Enrollment	ERLST	Enrollment start flag	<ERLST-CCAE>	4	147
		PLANTYP	Healthcare Plan type	<PLANTYP-5>	10	147
		CAP	Capitation flag	<CAP-1>	3	147
		EGEoloc	Geographic location	<EGEoloc-18>	68	147
		ERLED	Enrollment end flag	<ERLST-CCAE>	4	147
	Clinical code <sup>2</sup>	DX	Diagnosis (ICD-10-CM)	<DX-MAJOR_E11>	5,474	23,054
		PROC	Procedure (SNOMED CT, CPT-4)	<PROC-229315006>	12,473	17,319
		RX	Medication (Ingredient RxNorm)	<RX-1991302>	2,473	7,903
Expenditure	COST	Cost (aggregated and rounded)	<COST-23>	101	3,795	
Encounter specific	VT	visit type of claim	<VT-outpatient>	4	3,795	
	DS	Discharge status	<DS-1>	6	34	
	LS	Long stay ( $\geq 7$ days)	<LS-1>	3	34	
<b>Total</b>					<b>20,861</b>	<b>~62,000</b>

<sup>1</sup>Static tokens are not associated with any timestamp. Temporal tokens are aggregated at a specified temporal resolution and associated with a timestamp, so that they can be sorted chronologically.

<sup>2</sup>Clinical token counts are data-dependent.

**Table A9 | Walk-through of the example token sequence in Table A3.** Each row represents one logical token group. Rows alternate between time-interval markers (ATT-*N*, with  $\Delta$  giving elapsed months) and dated event groups (with calendar time).

Calendar Time	$\Delta$ (mo)	Event Type	Event Token Segment	Decoded Interpretation
		Sequence start	<sos>	Start of sequence.
		Demographics	<SEX-1>	Male.
Jan 1974		Birth year	<DOBYR-1974>	Year-of-birth anchor, placed at first month.
Jan 2018		Age (first event)	<AGE-44>	Age 44 at first recorded event (in 2018).
	0	Time interval	<ATT-0>	Same month (Jan 2018).
Jan 2018		Enrollment start	<ERLST-CCAE> <PLANTYP-6> <CAP-0> <EGEOLOC-04>	CCAE plan enrollment begins plan type: PPO non-capitated geographic region: Connecticut
	12	Time interval	<ATT-12>	Twelve months elapsed.
Jan 2019		New-year anchor	<NY>	Calendar-year boundary marker (2019).
	12	Time interval	<ATT-12>	Twelve months elapsed.
Jan 2020		New-year anchor	<NY>	Calendar-year boundary marker (2020).
	10	Time interval	<ATT-10>	Ten months elapsed.
Nov 2020		Outpatient visit	<VT-outpatient> <DX-PRINCIPAL> <DX-MAJOR_R07> <DX-MINOR_9> <DX-MAJOR_E11> <DX-MINOR_9> <PROC-PRINCIPAL> <PROC-COMBSTART> <PROC-268400002> <PROC-29303009> <PROC-308561006> <PROC-COMBEND> <PROC-165102003> <PROC-16254007> <PROC-COMBSTART> <PROC-408254005> <PROC-43396009> <PROC-COMBEND> <PROC-CPT499214> <COST-32>	Oupatient visit Principal diagnosis: - ICD10: R07.9 Chest pain - ICD10: E11.9 Type 2 diabetes mellitus Principal procedure: - Atomic SNOMED group mapped from CPT4:93000: Electrocardiogram, routine ECG with at least 12 leads; - SNOMED: Metabolic function test - SNOMED: Lipid panel - Atomic SNOMED group mapped from CPT4:83036: Hemoglobin; glycosylated (A1C) - CPT4 fallback: Established outpatient. Gross payment $\approx$ \$300
	0	Time interval	<ATT-0>	Same month (Nov 2020).
Nov 2020		Pharmacy visit	<VT-pharmacy> <RX-6809> <COST-51>	Pharmacy fill - RxNorm: 6809 Metformin Gross payment $\approx$ \$50.
	2	Time interval	<ATT-2>	Two months elapsed.
Jan 2021		New-year anchor	<NY>	Calendar-year boundary marker (2021).
	5	Time interval	<ATT-5>	Five months elapsed.
Jun 2021		Outpatient visit	<VT-outpatient> <DX-PRINCIPAL> <DX-MAJOR_I10> <PROC-PRINCIPAL> <PROC-165102003> <PROC-16254007> <PROC-COMBSTART> <PROC-408254005> <PROC-43396009> <PROC-COMBEND> <PROC-45896001> <PROC-34608000> <PROC-CPT499213> <COST-12>	Oupatient visit Principal diagnosis: - ICD10: I10 Essential Hypertension Principal procedure: - SNOMED: Metabolic function test - SNOMED: Lipid panel - Atomic SNOMED group mapped from CPT4:83036: Hemoglobin; glycosylated (A1C) - SNOMED: Aspartate aminotransferase - SNOMED: Alanine aminotransferase - CPT4 fallback: Established outpatient. Gross payment $\approx$ \$100
	0	Time interval	<ATT-0>	Same month.
Jun 2021		Pharmacy fill	<VT-pharmacy> <RX-18867> <RX-5487> <COST-51>	Pharmacy visit - RxNorm: 18867 Benazepril - RxNorm: 5487 Hydrochlorothiazide Gross payment $\approx$ \$50.
	1	Time interval	<ATT-1>	One month elapsed.

*Continued on next page*

Table A9 – continued from previous page

Calendar Time	$\Delta$ (mo)	Event Type	Token Segment	Decoded Interpretation
Jul 2021		Outpatient visit	<VT-outpatient> <DX-PRINCIPAL> <DX-MAJOR_E11> <DX-MINOR_9> <DX-MAJOR_E78> <DX-MINOR_2> <PROC-PRINCIPAL> <PROC-165102003> <PROC-16254007> <PROC-COMBSTART> <PROC-408254005> <PROC-43396009> <PROC-COMBEND> <PROC-63476009> <PROC-45896001> <PROC-34608000> <COST-22>	Oupatient visit Principal diagnosis: - ICD10: E11.9 Type 2 diabetes mellitus - ICD10: E78.2 Mixed hyperlipidemia Principal procedure: - SNOMED: Metabolic function test - SNOMED: Lipid panel - Atomic SNOMED group mapped from CPT4:83036: Hemoglobin; glycosylated (A1C) - SNOMED: Prostate specific antigen - SNOMED: Aspartate aminotransferase - SNOMED: Alanine aminotransferase Gross payment $\approx$ \$200
Jul 2021	0	Time interval	<ATT-0>	Same month (Jul 2021).
		Pharmacy visit	<VT-pharmacy> <RX-1991302> <RX-4018> <COST-23>	Pharmacy fill - RxNorm: 1991302 Semaglutide - RxNorm: 4018 Ergocalciferol Gross payment $\approx$ \$2,000.
Jan 2022	6	Time interval	<ATT-6>	Six months elapsed.
		New-year anchor	<NY>	Calendar-year boundary marker (2022).
Apr 2022	3	Time interval	<ATT-3>	Three months elapsed.
Apr 2022		Inpatient admission	<VT-inpatient> <DX-PRINCIPAL> <DX-MAJOR_R11> <DX-MINOR_2> <DX-SECONDARY> <DX-MAJOR_R10> <DX-MINOR_9> <DX-MAJOR_R13> <DX-MINOR_0> <DX-MAJOR_R13> <DX-MINOR_10> <DX-MAJOR_Z98> <DX-MINOR_84> <PROC-SECONDARY> <PROC-168702005> <PROC-241157000> <PROC-COMBSTART> <PROC-315639002> <PROC-86181006> <PROC-COMBEND> <DS-MISSING> <LS-0> <COST-43>	Inpatient admission Principal diagnosis: - ICD10: R11.2 Nausea with vomiting Secondary diagnosis: - ICD10: R10.9 Unspecified abdominal pain - ICD10: R13.0 Aphagia - ICD10: R13.10 Dysphagia - ICD10: Z98.84 Bariatric-surgery status Secondary procedure: - SNOMED: Plain X-ray of abdomen - SNOMED: Upper gastrointestinal tract series - Atomic SNOMED group mapped from CPT4:99231: Management of inpatient Discharge status: Unknown Stay < 7 days Gross payment $\approx$ \$4,000
Jan 2023	9	Time interval	<ATT-9>	Nine months elapsed.
		New-year anchor	<NY>	Calendar-year boundary marker (2023).
Apr 2023	3	Time interval	<ATT-3>	Three months elapsed.
Apr 2023		Outpatient visit	<VT-outpatient> <DX-PRINCIPAL> <DX-MAJOR_E11> <DX-MINOR_9> <PROC-PRINCIPAL> <PROC-165102003> <PROC-16254007> <PROC-COMBSTART> <PROC-408254005> <PROC-43396009> <PROC-COMBEND> <PROC-45896001> <PROC-COMBSTART> <PROC-117356000> <PROC-43789009> <PROC-COMBEND> <PROC-104154005> <PROC-CPT499214> <COST-22>	Oupatient visit Principal diagnosis: - ICD10: E11.9 Type 2 diabetes mellitus Principal procedure: - SNOMED: Metabolic function test - SNOMED: Lipid panel - Atomic SNOMED group mapped from CPT4:83036: Hemoglobin; glycosylated (A1C) - SNOMED: Aspartate aminotransferase - Atomic SNOMED group mapped from CPT4:85027: Obstetric panel - SNOMED: Erythrocyte sedimentation rate - CPT4 fallback: Established outpatient. Gross payment $\approx$ \$200
Dec 2023	8	Time interval	<ATT-8>	Eight months elapsed.
		Enrollment end	<ERLED-CCAE>	CCAE enrollment terminates.
		Sequence end	<eos>	End of sequence.

**Table A10** | Percentile of population ranked by healthcare expenditures during the year from MEPS-HC<sup>1</sup>

Percentile of Population	Annual healthcare expenditures (inflated to 2022 dollars)				
	2022	2021	2020	2019	2018
Top 1%	\$80,990 or more	\$92,906 or more	\$92,920 or more	\$88,632 or more	\$83,300 or more
Top 5%	\$30,206 or more	\$32,032 or more	\$30,650 or more	\$31,267 or more	\$30,402 or more
Top 10%	\$16,202 or more	\$17,250 or more	\$16,175 or more	\$17,214 or more	\$16,901 or more
Bottom 50%	Less than \$1,361	Less than \$1,471	Less than \$1,287	Less than \$1,490	Less than \$1,519

<sup>1</sup> Medical Expenditure Panel Survey Household Component (MEPS-HC).

**Table A11** | Key definitions for the target trial emulation

<b>Component</b>	<b>Definition</b>
Study population	Adults aged $\geq 18$ years with type 2 diabetes; excluding individuals with type 1 diabetes or end-stage renal disease or dialysis-related diagnoses during the baseline period
Study period	2019 – 2024
Treatment exposure	New initiation of one of three antidiabetic drug classes: glucagon-like peptide-1 receptor agonists (GLP-1 RAs), sodium–glucose cotransporter-2 inhibitors (SGLT-2is), or dipeptidyl peptidase-4 inhibitors (DPP-4is)
Index date	Date of the first observed prescription for any of the study drug classes
Baseline period	The 365-day period before the index date

**Table A12** | ICD-10-CM for Primary Psychiatric Outcomes

<b>Outcome</b>	<b>ICD-10-CM</b>
Depression	F32, F33
Anxiety disorders	F40, F41, F42, F43, F44, F45, F48
Bipolar disorder	F31
Schizophrenia and other psychotic disorders	F20, F21, F22, F23, F24, F25, F28, F29
Other mood disorders	F30, F34, F39
Suicidal ideation	V62.84, R45.851

**Table A13** | ICD-10-CM for Negative Control Outcomes

<b>Outcome</b>	<b>ICD-10-CM</b>	<b>Outcome</b>	<b>ICD-10-CM</b>
Abnormal posture	R29.3	Impingement syndrome of shoulder region	M75.4
Abnormal pupil	H21.56, H57.03, H57.0	Inadequate sleep hygiene	Z72.821
Abrasion and friction burn of multiple sites	T07	Ingrowing nail	L60.0
Abrasion and friction burn of trunk without infection	S00, S10, S20, S30, S40, S50, S60, S70, S80, S90	Injury of knee	S87.0
Absence of breast	Q83.0, Z90.1	Jellyfish poisoning	T63.62
Absent kidney	Q60, Z90.5	Kwashiorkor	E40
Acquired hallux valgus	M20.1	Lagophthalmos	H02.2
Acquired keratoderma	L85.1, L85.0, L11.0	Late effect of contusion	S00.83XS, S40.012S, S40.029S, S50.00XS, S50.10XS, S60.219S, S30.0XXS, S70.00XS, S80.00XS, S90.30XS
Anal and rectal polyp	K62.0, K62.1	Late effect of motor vehicle accident	V89.0XXS, V89.2XXS, V89.9XXS
Anomaly of jaw size	M26.0	Lipid storage disease	E75.6
Benign paroxysmal positional vertigo	H81.1	Lymphangioma	I89.1
Bizarre personal appearance	R46.1	Macular drusen	H35.36
Burn of forearm	T22.22	Malingering	Z76.5
Cachexia	R64	Marfan syndrome	Q87.4
Calcaneal spur	M77.3	Mechanical complication of internal orthopedic device implant graft	T84
Cannabis abuse	F12.1	Melena	K92.1
Changes in skin texture	R23.4	Minimal cognitive impairment	G31.84
Chondromalacia of patella	M22.4	Nicotine dependence	F17
Cocaine abuse	F14.1	Noise effects on inner ear	H83.3
Colostomy present	Z93.3, Z43.3	Nontoxic multinodular goiter	E04.2
Complication due to Crohn disease	K50.01, K50.11, K50.81, K50.91	Nonspecific tuberculin test reaction	R76.11
Complication of gastrostomy	K94.2	Opioid abuse	F11.1
Contact dermatitis	L23, L24, L25	Opioid intoxication	F11.12, F11.22, F11.92
Contusion of knee	S80.0	Passing flatus	R14.3
Crohn disease	K50	Physiological development failure	R62
Derangement of knee	M23	Poisoning by tranquilizer	T42.3, T42.4, T42.6
Developmental delay	R62, F88, F89	Postviral fatigue syndrome	G93.3
Deviated nasal septum	J34.2	Presbyopia	H52.4
Difficulty sleeping	G47, F51	Psychalgia	F45.41
Disproportion of reconstructed breast	N65.1	Ptotic breast	N64.81
Effects of hunger	T73.0XXA	Regular astigmatism	H52.22
Endometriosis	N80	Senile hyperkeratosis	L57.0
Epidermoid cyst	L72.0	Social exclusion	Z60.4

*Continued on next page*

Table A13 – continued from previous page

<b>Outcome</b>	<b>ICD-10-CM</b>	<b>Outcome</b>	<b>ICD-10-CM</b>
Exhaustion due to excessive exertion	T73.3XXA	Somatic dysfunction of lumbar region	M99.03
Feces contents abnormal	R19.5	Splinter of face without major open wound	S00.85
Foreign body in ear	T16	Sprain of ankle	S93.4
Foreign body in orifice	W44	Strain of rotator cuff capsule	S43.42
Foreskin deficient	N47.3	Symbolic dysfunction	R48
Galactosemia	E74.21	Tear film insufficiency	H04.12
Ganglion cyst	M67.4	Tobacco dependence syndrome	F17.2
Genetic disorder carrier	Z14	Tooth loss	K08.1, K08.4
Hammer toe	M20.4	Toxic effect of lead compound	T56.0
Hereditary thrombophilia	D68.1	Toxic effect of tobacco and nicotine	T65.2
High risk sexual behavior	Z72.5	Tracheostomy present	Z93.0
Homocystinuria	E72.11	Unsatisfactory tooth restoration	K08.5
Impacted cerumen	H61.2		

**Table A14** | Configurations for the three ReClaim models trained from scratch with our custom tokenizer and vocabulary.

<b>Configuration</b>	<b>Qwen3-S (140M)</b>	<b>Qwen3-M (700M)</b>	<b>Qwen3-L (1.7B)</b>
Hidden size ( $d_{\text{model}}$ )	1,024	2,048	2,048
Transformer layers ( $L$ )	8	16	32
Attention heads ( $n_{\text{head}}$ )	16	24	32
Key-value heads ( $n_{\text{kv}}$ )	8	12	16
Intermediate size ( $d_{\text{ffn}}$ )	2,048	4,096	4,096
Max position embeddings	4,096	4,096	4,096
Vocabulary size	20,865	20,865	20,865

**Table A15** | Disease endpoints where post-training AUC is lower than pre-training AUC (25 of 1,208 endpoints; 2.1%). Sorted by  $\Delta$ AUC (post – pre), most negative first. Pre and Post columns report disease-level AUC (%) for ReClaim-L before and after task-specific post-training;  $\Delta$  is the percentage-point change;  $N_+$  is the number of positive cases in the held-out test cohort; Prev is the percentage of post-training enrollees whose medical history sequence contains the ICD code at least once; Freq is the total number of times the ICD code appears across all post-training sequences, counting repeated occurrence within the same enrollee. N.A. indicates that the corresponding ICD code was not present in the post-training data. For many of the endpoints with degraded performance, the corresponding ICD codes have very low prevalence and frequency in the post-training data, suggesting that the performance drop may be partially explained by limited post-training exposure to these diseases.

ICD	Disease	Chapter	Pre (%)	Post (%)	$\Delta$ (pp)	$N_+$	Prev (%)	Freq
B81	Other intestinal helminthiases, not elsewhere classified	I. Infectious Diseases	76.08	54.66	-21.42	10	0.0060	6
P13	Birth injury to skeleton	XVI. Perinatal Conditions	79.77	65.65	-14.12	3	0.0040	4
E68	Sequelae of hyperalimentation	IV. Metabolic Diseases	94.61	81.87	-12.74	2	N.A	N.A
B42	Sporotrichosis	I. Infectious Diseases	70.71	58.15	-12.56	13	0.0030	3
D77	Other disorders of blood and blood-forming organs in diseases classified elsewhere	III. Blood & Immune Disorders	84.19	74.52	-9.67	2	-	-
C33	Malignant neoplasm of trachea	II. Neoplasms	77.82	68.42	-9.41	30	0.0060	6
E45	Retarded development following protein-energy malnutrition	IV. Metabolic Diseases	79.65	70.37	-9.28	4	0.0040	7
A55	Chlamydial lymphogranuloma venereum	I. Infectious Diseases	68.88	63.08	-5.80	7	0.0030	4
A94	Unspecified arthropod-borne viral fever	I. Infectious Diseases	71.54	65.79	-5.76	2	0.0020	3
B68	Taeniasis	I. Infectious Diseases	61.70	56.62	-5.09	19	0.0040	4
P50	Foetal blood loss	XVI. Perinatal Conditions	67.37	63.36	-4.01	5	0.0010	7
G14	Postpolio syndrome	VI. Nervous System Diseases	53.97	50.32	-3.65	67	0.0220	42
A67	Pinta [carate]	I. Infectious Diseases	66.46	63.30	-3.16	6	N.A	N.A
P25	Interstitial emphysema and related conditions originating in the perinatal period	XVI. Perinatal Conditions	68.54	66.05	-2.49	18	0.0030	7
O21	Excessive vomiting in pregnancy	XV. Pregnancy & Childbirth	72.65	70.24	-2.41	3,395	1.0520	1,486
B91	Sequelae of poliomyelitis	I. Infectious Diseases	75.72	73.34	-2.37	66	0.0220	44
O60	Preterm delivery	XV. Pregnancy & Childbirth	70.72	68.44	-2.28	4,497	1.5840	3,433
O25	Malnutrition in pregnancy	XV. Pregnancy & Childbirth	81.80	79.65	-2.15	5,318	2.2470	6,587
L14	Bullous disorders in diseases classified elsewhere	XII. Skin Diseases	98.06	96.44	-1.63	1	-	-
J62	Pneumoconiosis due to dust containing silica	X. Respiratory Diseases	87.45	85.86	-1.59	28	0.0070	7
C66	Malignant neoplasm of ureter	II. Neoplasms	75.07	73.85	-1.23	65	0.0170	23
A82	Rabies	I. Infectious Diseases	67.03	66.01	-1.02	21	0.0020	3
K67	Disorders of peritoneum in infectious diseases classified elsewhere	XI. Digestive Diseases	83.13	82.45	-0.68	8	0.0010	1
O44	Placenta praevia	XV. Pregnancy & Childbirth	64.27	64.21	-0.05	1,796	0.5030	2,429
O02	Other abnormal products of conception	XV. Pregnancy & Childbirth	67.46	67.45	-0.01	3,404	0.9260	1,238

**Table A16** | Primary psychiatric outcome estimates before and after negative control outcome calibration across treatment comparisons and model specifications.

Treatment vs Control	Primary outcome	Embeddings	No. of Events/N		RR (95% CI)	
			Treatment	Control	Before Calibration	After Calibration
GLP-1RA vs DPP-4i	Depression	No embedding	168/1115	190/1115	0.88 (0.73–1.07)	1.00 (0.69–1.45)
		Delphi	173/1105	189/1105	0.92 (0.76–1.11)	1.06 (0.81–1.38)
		ReClaim-L	169/927	166/927	1.02 (0.84–1.24)	0.98 (0.80–1.19)
	Anxiety disorders	No embedding	235/1115	237/1115	0.99 (0.84–1.16)	1.12 (0.79–1.60)
		Delphi	239/1105	236/1105	1.01 (0.86–1.19)	1.17 (0.91–1.49)
		ReClaim-L	227/927	210/927	1.08 (0.92–1.27)	1.04 (0.88–1.22)
	Bipolar disorder	No embedding	21/1115	32/1115	0.66 (0.38–1.13)	0.74 (0.40–1.39)
		Delphi	31/1105	32/1105	0.97 (0.60–1.58)	1.12 (0.66–1.88)
		ReClaim-L	21/927	27/927	0.78 (0.44–1.37)	0.75 (0.43–1.31)
	Schizophrenia	No embedding	4/1115	24/1115	0.17 (0.06–0.48)	0.19 (0.06–0.57)
		Delphi	5/1105	24/1105	0.21 (0.08–0.54)	0.24 (0.09–0.64)
		ReClaim-L	5/927	19/927	0.26 (0.10–0.70)	0.25 (0.09–0.67)
	Other mood disorders	No embedding	20/1115	23/1115	0.87 (0.48–1.57)	0.98 (0.50–1.93)
		Delphi	15/1105	22/1105	0.68 (0.36–1.31)	0.79 (0.40–1.55)
		ReClaim-L	20/927	20/927	1.00 (0.54–1.85)	0.96 (0.52–1.77)
Suicidal ideation	No embedding	39/1115	41/1115	0.95 (0.62–1.46)	1.08 (0.63–1.84)	
	Delphi	33/1105	43/1105	0.77 (0.49–1.20)	0.88 (0.55–1.44)	
	ReClaim-L	36/927	34/927	1.06 (0.67–1.68)	1.02 (0.64–1.61)	
GLP-1RA vs SGLT2i	Depression	No embedding	305/2052	326/2052	0.94 (0.81–1.08)	1.02 (0.80–1.29)
		Delphi	325/2049	322/2049	1.01 (0.88–1.16)	1.08 (0.86–1.34)
		ReClaim-L	296/1839	303/1839	0.98 (0.84–1.13)	0.97 (0.84–1.12)
	Anxiety disorders	No embedding	438/2052	458/2052	0.96 (0.85–1.07)	1.04 (0.83–1.29)
		Delphi	424/2049	458/2049	0.93 (0.82–1.04)	0.99 (0.80–1.21)
		ReClaim-L	397/1839	435/1839	0.91 (0.81–1.03)	0.91 (0.80–1.02)
	Bipolar disorder	No embedding	45/2052	55/2052	0.82 (0.55–1.21)	0.89 (0.58–1.37)
		Delphi	41/2049	54/2049	0.76 (0.51–1.13)	0.81 (0.52–1.25)
		ReClaim-L	46/1839	53/1839	0.87 (0.59–1.28)	0.86 (0.58–1.27)
	Schizophrenia	No embedding	6/2052	28/2052	0.21 (0.09–0.52)	0.23 (0.09–0.57)
		Delphi	10/2049	28/2049	0.36 (0.17–0.73)	0.38 (0.18–0.80)
		ReClaim-L	9/1839	26/1839	0.35 (0.16–0.74)	0.34 (0.16–0.73)
	Other mood disorders	No embedding	37/2052	31/2052	1.19 (0.74–1.92)	1.30 (0.78–2.16)
		Delphi	44/2049	30/2049	1.47 (0.93–2.32)	1.56 (0.96–2.55)
		ReClaim-L	40/1839	27/1839	1.48 (0.91–2.40)	1.47 (0.91–2.39)
Suicidal ideation	No embedding	65/2052	54/2052	1.20 (0.84–1.72)	1.31 (0.87–1.95)	
	Delphi	64/2049	53/2049	1.21 (0.84–1.73)	1.29 (0.86–1.91)	
	ReClaim-L	63/1839	52/1839	1.21 (0.84–1.74)	1.20 (0.84–1.73)	
SGLT2i vs DPP-4i	Depression	No embedding	197/1164	200/1164	0.98 (0.82–1.18)	1.14 (0.85–1.53)
		Delphi	171/1157	198/1157	0.86 (0.72–1.04)	1.03 (0.76–1.41)
		ReClaim-L	180/1033	172/1033	1.05 (0.87–1.27)	1.06 (0.82–1.39)
	Anxiety disorders	No embedding	275/1164	254/1164	1.08 (0.93–1.26)	1.25 (0.95–1.66)
		Delphi	268/1157	250/1157	1.07 (0.92–1.25)	1.28 (0.96–1.71)
		ReClaim-L	257/1033	217/1033	1.18 (1.01–1.39)	1.20 (0.94–1.54)
	Bipolar disorder	No embedding	25/1164	34/1164	0.74 (0.44–1.22)	0.85 (0.48–1.49)
		Delphi	27/1157	34/1157	0.79 (0.48–1.31)	0.95 (0.54–1.66)
		ReClaim-L	36/1033	28/1033	1.29 (0.79–2.09)	1.31 (0.78–2.20)
	Schizophrenia	No embedding	16/1164	28/1164	0.57 (0.31–1.05)	0.66 (0.34–1.27)
		Delphi	12/1157	27/1157	0.44 (0.23–0.87)	0.53 (0.26–1.09)
		ReClaim-L	17/1033	24/1033	0.71 (0.38–1.31)	0.72 (0.38–1.37)
	Other mood disorders	No embedding	21/1164	24/1164	0.88 (0.49–1.56)	1.01 (0.54–1.89)
		Delphi	15/1157	24/1157	0.62 (0.33–1.19)	0.75 (0.38–1.48)
		ReClaim-L	16/1033	20/1033	0.80 (0.42–1.54)	0.81 (0.41–1.60)
Suicidal ideation	No embedding	28/1164	43/1164	0.65 (0.41–1.04)	0.75 (0.45–1.27)	
	Delphi	33/1157	44/1157	0.75 (0.48–1.17)	0.90 (0.54–1.49)	
	ReClaim-L	33/1033	41/1033	0.80 (0.51–1.26)	0.82 (0.50–1.33)	

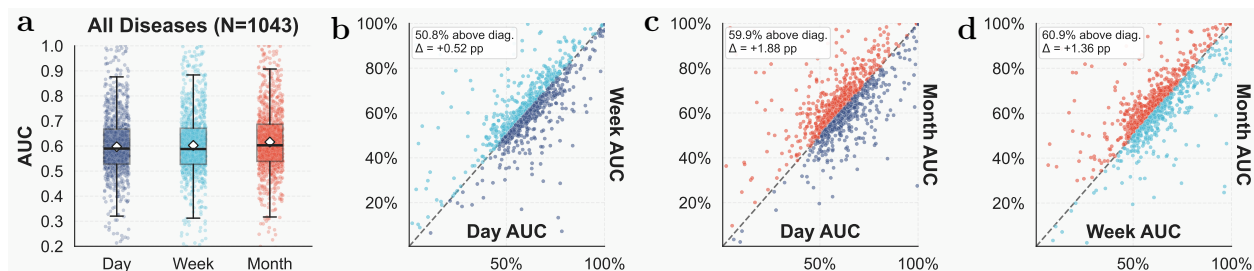


**Figure A1 | Coarser temporal-resolution encoding favors the Month variant.** Comparison of three temporal-encoding granularities (Day, Week, Month) used to discretize inter-event intervals in the patient-trajectory representation. All three variants are ReClaim-S models pre-trained on the full MarketScan training corpus and evaluated on a 100,000-patient held-out validation cohort. Disease tokens were harmonized across encodings via the canonical `<DX-MAJOR_*>` identifier, yielding 1,043 disease endpoints shared by all three variants; all panels use this 3-way intersection. (a), Distribution of disease-level AUC for the Day, Week, and Month encodings, shown as box plots with overlaid jittered scatter; diamonds indicate group means. Mean (median) AUC was 59.73% (58.99%) for Day, 60.26% (58.82%) for Week, and 61.61% (60.30%) for Month, identifying Month as the strongest variant overall. (b), Per-disease paired scatter of Week AUC versus Day AUC; the two encodings are largely comparable, with Week exceeding Day in 50.8% of endpoints (mean  $\Delta = +0.52$  pp). (c), Per-disease paired scatter of Month AUC versus Day AUC; the Month encoding exceeds the Day encoding in 59.9% of endpoints (mean  $\Delta = +1.88$  pp). (d), Per-disease paired scatter of Month AUC versus Week AUC; the Month encoding exceeds the Week encoding in 60.9% of endpoints (mean  $\Delta = +1.36$  pp). Together, these comparisons identify Month as the preferred temporal-resolution choice: it delivers the highest mean and median AUC and outperforms both Day and Week in the majority of disease endpoints, while at the same time producing the shortest patient-level token sequence among the three variants and therefore the lowest computational and context-length cost during pre-training and inference.

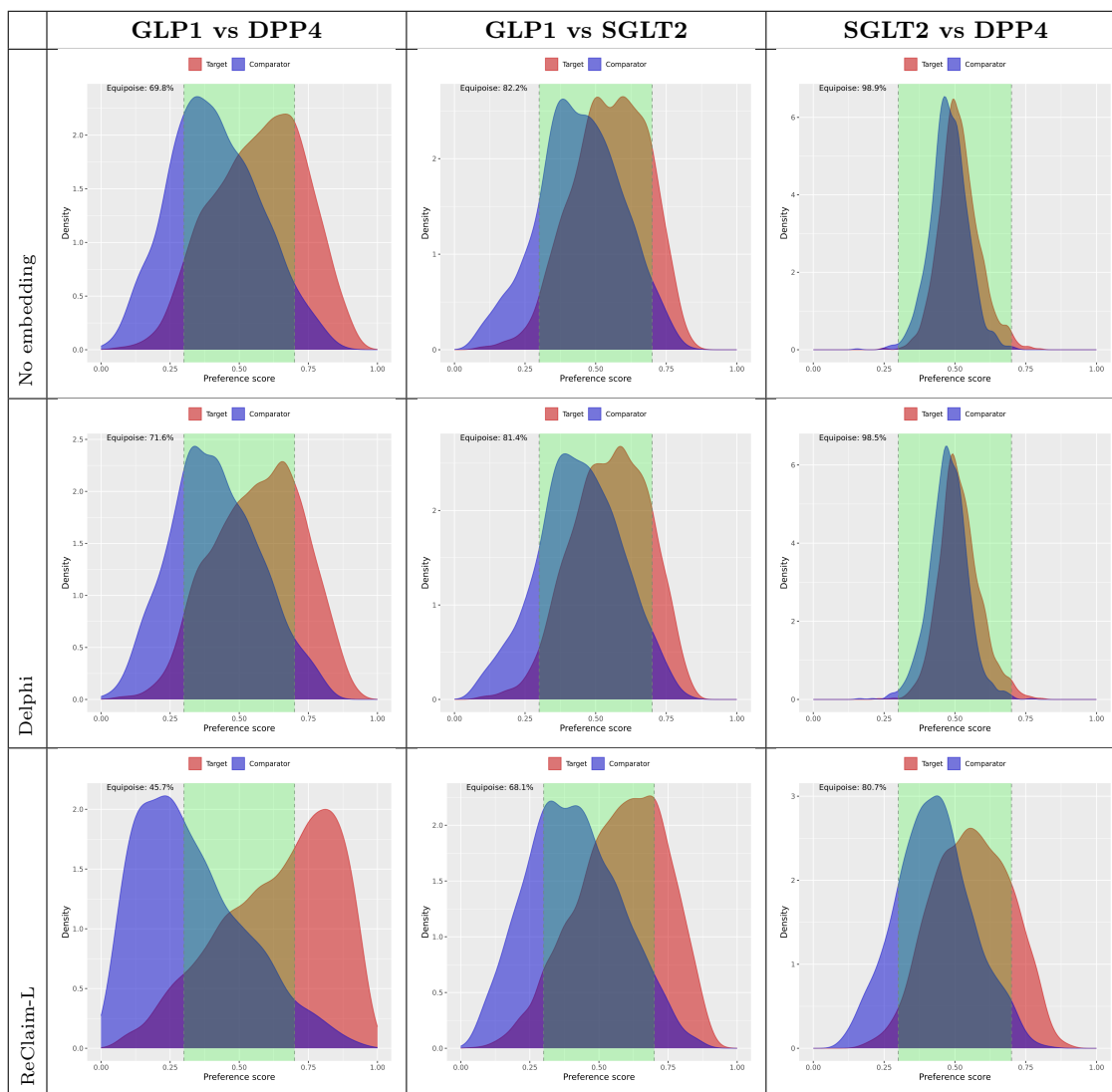


**Figure A2 | Equipoise plots after propensity score matching across pairwise treatment comparisons.** Columns represent pairwise treatment comparisons among glucagon-like peptide-1 receptor agonists (GLP-1 RAs), sodium-glucose cotransporter-2 inhibitors (SGLT-2is), and dipeptidyl peptidase-4 inhibitors (DPP-4is), while rows denote the model-derived embedding variants used for propensity score estimation.